

No Catalytic Performance Analysis of Gasoline Engine Tapered Variable Cell Density Carrier Catalytic Converter

Qingsong Zuo

Xiangtan University

Xiaomei Yang (✉ 313236787@qq.com)

Xiangtan University <https://orcid.org/0000-0002-4003-469X>

Bin Zhang

Xiangtan University

Qingwu Guan

Technique center.Hunan Tyen Machinery Co

Zhuang Shen

Xiangtan University

Yongchuan Xie

Xiangtan University

Qiming Li

Xiangtan University

Research Article

Keywords: Catalytic converter, NO catalysis, NO₂ mass fraction, vehicle emission, Gas uniformity, Pressure drops

Posted Date: May 27th, 2021

DOI: <https://doi.org/10.21203/rs.3.rs-458071/v1>

License: © ⓘ This work is licensed under a Creative Commons Attribution 4.0 International License.

[Read Full License](#)

Version of Record: A version of this preprint was published at Environmental Science and Pollution Research on August 5th, 2021. See the published version at <https://doi.org/10.1007/s11356-021-15504-y>.

NO Catalytic Performance Analysis of Gasoline Engine Tapered Variable Cell Density Carrier Catalytic Converter

Qingsong Zuo^a, Xiaomei Yang^a, Bin Zhang^a*, Qingwu Guan^b, Zhuang Shen^a, Yongchuan Xie^a,

Qiming Li^a

a. School of Mechanical Engineering, Xiangtan University, Xiangtan, 411105, China

b. Technique Center, Hunan Tyen Machinery Co., Ltd., Hengyang, 421000, China

Institute of Engineering, Xiangtan 411104, China

* binzhang0627@xtu.edu.cn.

Abstract: Improving the flow field uniformity of catalytic converter can promote the catalytic conversion of NO to NO₂. Firstly, the physical and mathematical models of improved catalytic converter are established, and its accuracy is verified by experiments. Then, the NO catalytic performance of standard and improved catalytic converters is compared, and the influences of structural parameters on its performance are investigated. The results showed that: (1) The gas uniformity, pressure drop and NO conversion rate of the improved catalytic converter are increased by 0.0643, 6.78% and 7.0% respectively. (2) As the cell density combination is 700 cpsi/600 cpsi, NO conversion rate reaches the highest, 73.7%, and the gas uniformity is 0.9821. (3) When the tapered height is 20 mm, NO conversion rate reaches the highest, 72.4%, the gas uniformity is 0.9744. (4) When the high cell density radius is 20 mm, NO conversion rate reaches the highest, 72.1%, the gas uniformity is 0.9783. (5) When the tapered end face radius is 20 mm, NO conversion rate reaches the highest, 72.0%, the gas uniformity is 0.9784. The results will provide a very important reference value for improving NO catalytic and reducing vehicle emission.

Keywords: Catalytic converter; NO catalysis; NO₂ mass fraction; vehicle emission; Gas uniformity; Pressure drops

23 1. Introduction

24 Environmental pollution brings serious ecological problems (Matsuzawa et al. 2001; Baumard et al.
25 1998), and automobile exhaust pollution is one of the sources of serious environmental pollution, so it is
26 urgent to reduce automobile emissions (Zhang et al. 2021; Sun et al. 2021; Lichtfouse et al. 1997). Many
27 countries have formulated strict emission standards to improve environmental quality (Qian et al. 2019a,
28 2019b; Park et al. 2019). At present, some ways to reduce emission pollution, such as improving fuel,
29 combustion mode and adding post-processor have been proposed (Zhong et al. 2018, 2016). Among them,
30 catalytic converters have been proved to be an indispensable device to reduce automobile exhaust pollutants
31 (E et al. 2020; Manojkumar et al. 2020; Subhashish et al. 2019). Previous studies have shown that catalytic
32 converters can reduce 95% CO, HC and NO_x under the condition that the operating environment meets the
33 requirements (Santos et al. 2008; Matthew et al. 2016). However, due to the uneven flow field in the
34 standard catalytic converter in practice, the purification of pollutants is limited (Mu et al. 2019a; Shen et al.
35 2019). Besides, it also causes sintering of the catalyst, affecting its later use (Gao et al. 2019; Liang et al.
36 2019). Therefore, it is necessary to further improve the uniformity of flow field in catalytic converters
37 (Andrew et al. 2014).

38 For catalytic converters, Hesham et al. (2018) proposed that insulating material was placed in the
39 carrier channel to investigate the distribution of the internal flow field. They found that the gas uniformity
40 was improved by 5%. Day et al. (2020) surveyed various catalysts in catalytic converters. They revealed
41 that compared with noble metal catalysts, Cu was the most powerful and active catalyst for CO. Mu et al.
42 (2019b) proposed a rationalized B-spline expansion pipe structure. The results revealed that the pressure
43 drop was reduced by 12%, and the gas uniformity was better. Miles et al (2017) researched Alumina with
44 3 nm cerium dioxide nanoparticles (ceria NPs). The research indicated that supported 3 nm ceria NPs were
45 found to lower the light-off temperature for CO by 200 and 100°C compared to inactivated and activated

46 ceria micro-powders, respectively. Almeida et al. (2014) investigated the impact of temperature on the aging
47 of catalytic converters, and claimed that higher temperatures would reduce the conversion efficiency and
48 accelerate the aging of the catalytic converters. Liu et al. (2020) measured the distribution of catalytic
49 converter particles by DMS500 and analyzed the particle characteristics. The results showed that TWC
50 could reduce particles by 20-35% and GPF by 70-85%. Liu et al. (2021) studied the effect of exhaust gas
51 temperature on the purification of particulate matter. The results showed that after the exhaust gas passed
52 through the catalytic converter, the particles of 4-8 nm were reduced by 96%, while the purification effect
53 of particles larger than 50 nm was not obvious. Ayodhya et al. (2018) studied the arrangement order of post-
54 processing equipment. The results showed that a good after-treatment setup should have its devices placed in the
55 order: Diesel oxidation catalyst followed by Diesel particulate filter and Selective catalytic reduction. Bogarra
56 et al. (2017) studied the catalysis of HC compounds, and found that when the temperature reached 350°C,
57 HC compounds could effectively catalyze and effectively reduce the particles less than 20 nm. Kumar et al.
58 (2019) carried out experiments on diesel methanol nitromethane mixture. The results showed that the best
59 performance and emission results were observed when diesel oil was 92.5%, methanol was 5% and
60 nitromethane was 2.5%. Zhong et al. (2021) studied the influence of NO₂ / NO_x ratio on diesel particulate filter.
61 the catalytic performance of NO conversion was limited by mass transfer in Diesel oxidation catalyst catalytic
62 coating, while it was almost non-existent in catalytic diesel particulate filter.

63 In summary, at present, some scholars have paid attention to the flow characteristics of catalytic
64 converters, but more attention was paid to the influence of different factors on catalytic converters. Takeru
65 et al. (2017) found, compared with the standard carrier structure, the catalyst durability of the radial variable
66 cell density carrier was better, and the NO_x reaction temperature was reduced by 10°C. Xu et al. (2009)
67 claimed the structure of the tapered end-face carrier was more favorable to the uniformity of exhaust.
68 Considering the actual problems of purification effect and catalyst sintering, a more optimized catalytic

69 converter model must establish.

70 Therefore, the improved catalytic converter model with tapered end face radial variable cell density
71 carrier is established, and its accuracy is verified by experiments in this work. Then, the purification
72 performance and flow characteristic of standard and improved catalytic converters are compared, and the
73 effects of different structural parameters on the improved catalytic converter are analyzed. Finally, the gray
74 correlation analysis method is used to explore the influence degree of different structural parameters. To
75 achieve the goal of homogenizing the flow field in the catalytic converter and improving the purification
76 performance. The research results will provide a very important reference value for improving the
77 purification performance and service life of catalytic converters.

78 **2. Model construction and performance comparative analysis**

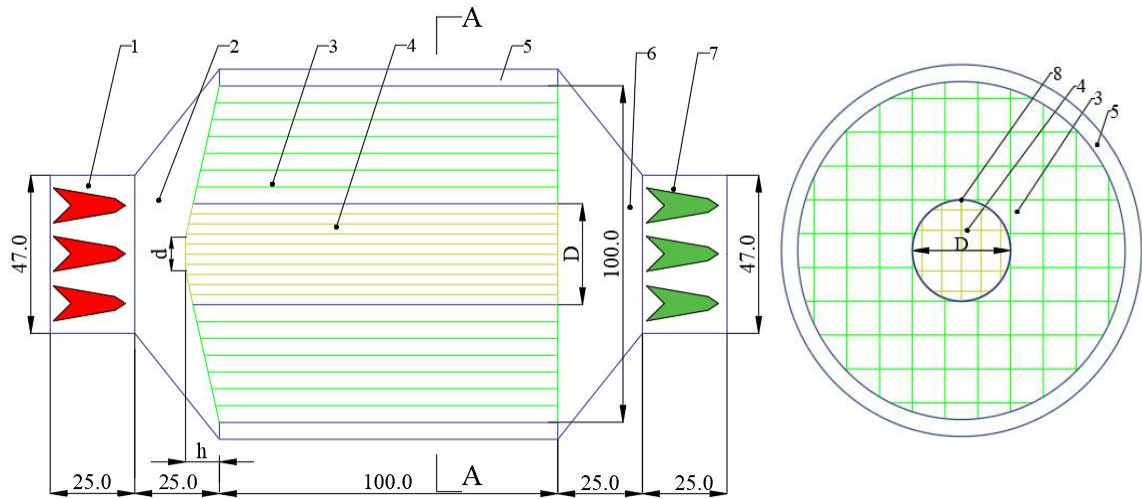
79 *2.1. Geometric model*

80 The geometrical model of the improved catalytic converter is shown in **Fig. 1**, and the parameters are
81 shown in **Table 1**. The exhaust flows in from the inlet pipe, and some exhaust flows to the edge of the
82 carrier under the action of the expansion pipe and the tapered end face. In addition, the resistance of the
83 medium carrier with high cell density is greater than that of the edge, which makes the exhaust flows to the
84 edge with less resistance. The carriers are all porous media, the surface of which is coated with precious
85 metal catalyst Pt, and the pollutants are catalyzed in the carrier area to achieve purification. Finally, exhaust
86 is discharged from the outlet pipe.

87 **Table 1** Carrier structure parameters

Item	Values
Tapered height (h)	10 mm
Tapered end face diameter (d)	10 mm

High cell density carrier diameter (D)	30 mm
High /Low cell density	500 cpsi/400 cpsi
High /Low specific surface area	2995/2728
High /Low porosity	72%/75%



88

89

1-inlet pipe, 2-expansion pipe, 3-low cell density carrier, 4-high cell density carrier,

90

5-liner, 6-contraction pipe, 7-outlet pipe, 8-interface of high and low cell density

91

Fig. 1 Structure of tapered variable cell density carrier catalytic converter

92 2.2. Mathematical model

93

To facilitate the establishment of mathematical model, it is necessary to make reasonable assumptions

94

to simplify the model, as follow: (a) No heat loss of steel shell and liner; (b) The exhaust is an

95

incompressible ideal gas; (c) Only 8 kinds of exhaust components: NO, H₂O, N₂, O₂, CO₂, CO, HC and

96

NO₂; (d) All reactions occur only on the surface of the carrier (Zuo et al. 2019a).

97

(1) Carrier pressure drop

98

The carrier region is a fully developed laminar flow, which is simulated as a porous medium, making

99

it an additional pressure loss term of the flow momentum equation (Su et al. 2013):

$$S_i = \frac{\partial p}{\partial x_i} = -\left(\sum_{j=1}^3 F_{ij} u v_j + \sum_{j=1}^3 C_{ij} \frac{1}{2} \rho |v_j| v\right) \quad (1)$$

Where p is pressure, Pa; u is dynamic viscosity, Pa·s; v is the velocity, m·s⁻¹; ρ is gas density, kg·m⁻³; F and C are viscosity and inertia loss coefficient matrices respectively; i, j are the direction of x, y, and z in the rectangular coordinate system.

The total carrier pressure drop mainly includes Δp_1 caused by the friction of carrier channel and Δp_2 caused by the inlet and outlet of the channel (Su et al. 2013).

$$\Delta p_1 = \frac{A \cdot \mu \cdot v \cdot L}{d_h^2} \quad (2)$$

$$\Delta p_2 = \frac{B}{2} \rho v^2 \quad (3)$$

Where for uncoated square channel $A=28.4$; d_h is hydraulic diameter of carrier channel, m; L is the maximum length of carrier, m; the coefficient B is 0.5.

(2) Reaction mechanism (Zuo et al. 2019b)

(a) NO catalyzed reaction:



(b) Reaction rate equation:

$$K = \alpha \exp\left(-\frac{E}{R_0 T}\right) \quad (5)$$

Where K is the reaction rate, α is the pre-factor, mol·K·(m²·s)⁻¹; E is reaction activation energy, J·mol⁻¹; R_0 is the universal gas constant, $R_0=8.314$ J·(mol·K)⁻¹; T is the exhaust temperature, K.

(3) Composition conservation equation (Deng et al. 2017):

$$\frac{\partial(\rho u Y_\beta)}{\partial x} + \frac{\partial(\rho v Y_\beta)}{\partial y} = -\left[\frac{\partial}{\partial x}(\rho S_\beta \frac{\partial Y_\beta}{\partial x}) + \frac{\partial}{\partial y}(\rho S_\beta \frac{\partial Y_\beta}{\partial y})\right] + R_\beta \quad (6)$$

Where Y_β is the mass fraction of component β , %; S_β is the diffusion coefficient of component β , m²·s⁻¹; R_β

121 is the formation or consumption rate of component β , $\text{kmol}\cdot(\text{m}^3\cdot\text{s})^{-1}$.

122 Exhaust uniformity is measured by exhaust uniformity index γ (Su et al. 2013):

$$123 \quad \gamma = 1 - \frac{1}{2n} \sum_{t=1}^n \frac{\sqrt{(v_t - v_m)^2}}{v_m} \quad (7)$$

124 Where n is the number of carrier channels; v_t and v_m are respectively the velocity of channel t and the
125 average velocity of the carrier; The γ value varies between 0 and 1.0, and the closer it is to 1.0, the more
126 uniform the flow will be.

127 No conversion rate η (Zuo et al. 2019b):

$$128 \quad \eta = \frac{\text{NO}_{\text{in}} - \text{NO}_{\text{out}}}{\text{NO}_{\text{in}}} \quad (8)$$

129 Where NO_{in} is the quality fraction of imported NO and NO_{out} is the quality fraction of exported NO.

130 The catalytic reaction mechanism of NO is shown in **Table 2** (Deng et al. 2017).

131 **Table 2** NO-O₂ reaction mechanism

No.	Elementary reactions	Pre-exponential(s^{-1})	Activation energy(kJ/mol)
R_1	$\text{NO} + 1/2\text{O}_2 \rightarrow \text{NO}_2$	9e+11	110.9
R_2	$\text{NO}_2 \rightarrow \text{NO} + 1/2\text{O}_2$	3.2e+12	162

132 2.3. Simulated boundary conditions

133 The computational fluid dynamics software Fluent is used to simulate the catalytic converter. In the
134 flow and combustion models, the standard k - ϵ model and the species transport model are selected to solve
135 the flow and chemical reaction models respectively. The second-order upwind scheme is selected to
136 discretize each governing equation. The residual error of energy equation is 1×10^{-6} , while the residual errors
137 of the other equations are 1×10^{-3} (Cai et al. 2020). The inlet temperature is 575 K, and the inlet velocity is
138 $10.28 \text{ m}\cdot\text{s}^{-1}$, $6.12 \text{ m}\cdot\text{s}^{-1}$ and $4.93 \text{ m}\cdot\text{s}^{-1}$, respectively. Setting outlet boundary condition as pressure outlet.

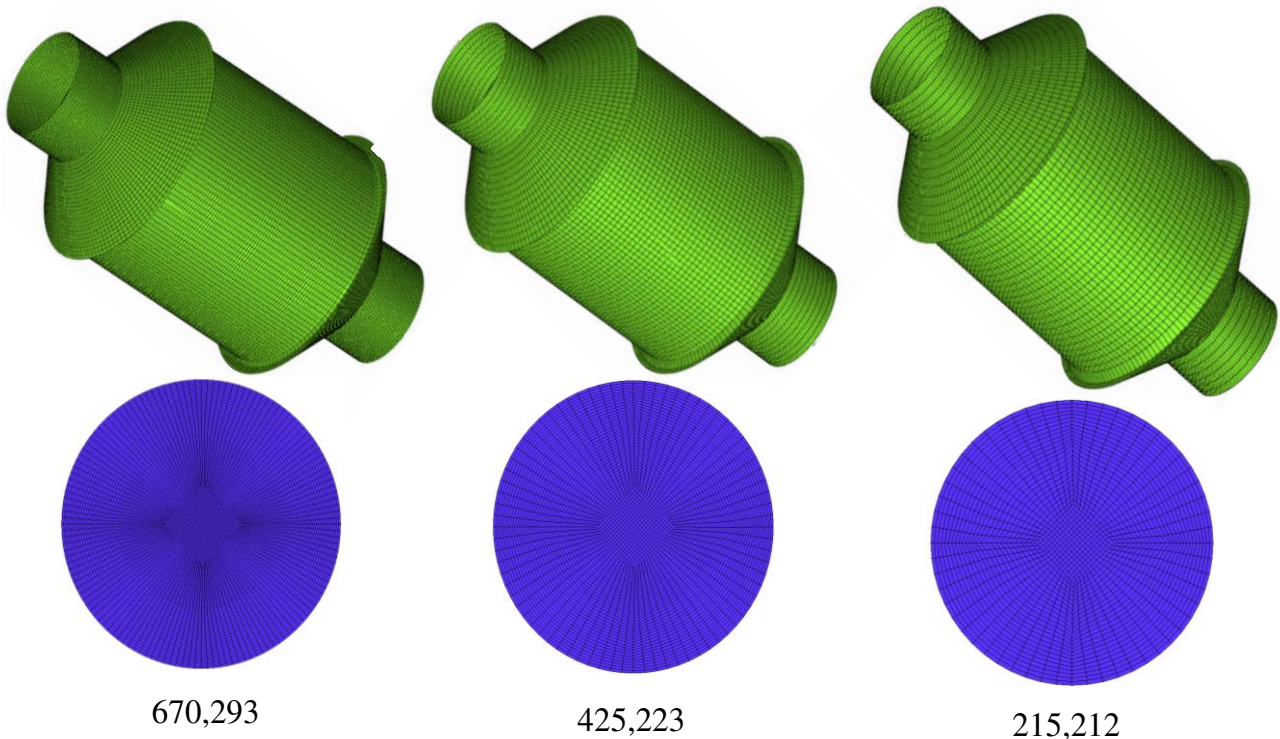
139 The composition and content of the inlet exhaust are shown in **Table 3** (Deng et al. 2017).

Table 3 Inlet exhaust composition and mass fraction

NO(%)	O ₂ (%)	H ₂ O(%)	C ₃ H ₆ (%)	CO(%)	CO ₂ (%)	N ₂ (%)
0.08	1.4	12.31	0.08	0.35	26.75	59.03

141 *2.4. Grid independence analysis*

142 To determine the appropriate mesh number, the impact of different mesh number models on the
 143 simulation results should be study. Three mesh models with different grids numbers are established,
 144 respectively 670,293, 425,223 and 215,212, as shown in **Fig. 2**. For the convenience of analysis, the total
 145 axis length of the catalytic converter is defined as Z , and the distance from a point on the axis to the inlet is
 146 defined as z , then the dimensionless distance expressed as z/Z . The radius of the carrier is R , and the distance
 147 from a point to the central axis is r , then the radius dimensionless distance is expressed as r/R .



148

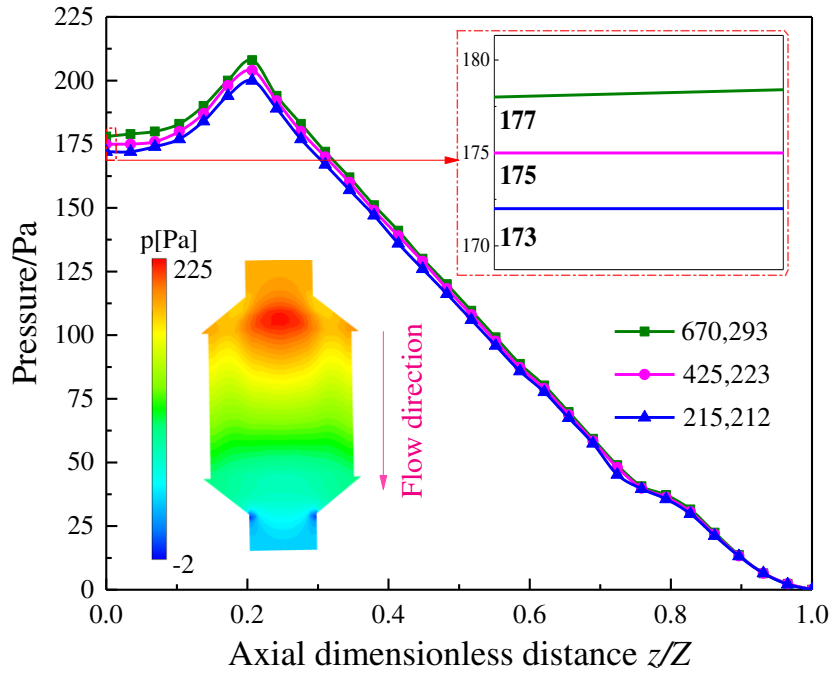
149

Fig. 2 Three different mesh models

150

The simulation results are shown in **Fig. 3**. The pressure and velocity distribution trends in the three

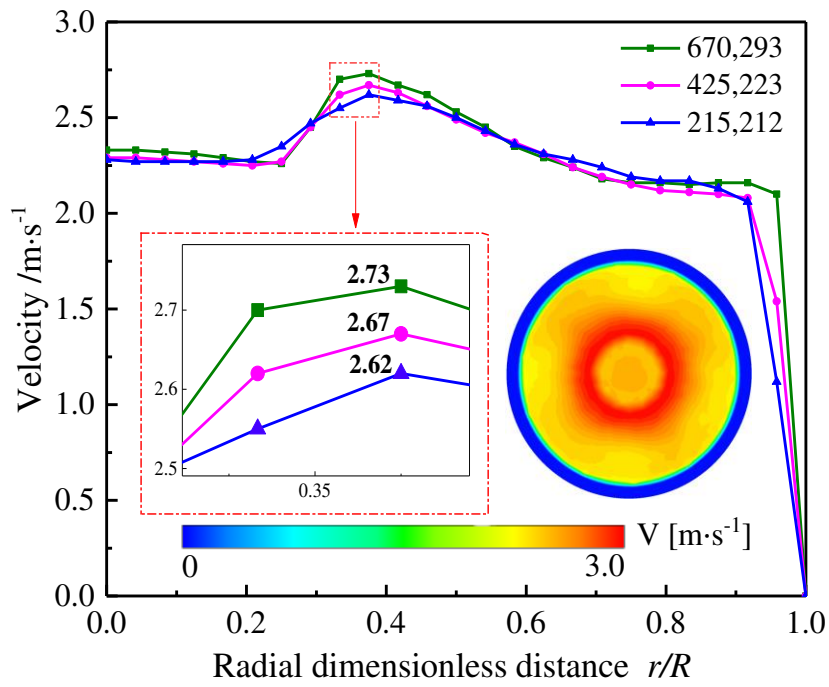
151 different mesh models are all the same, and the values differ little, all less than 5%. Considering the
 152 calculation time and the accuracy of numerical results (Zhao et al. 2019; Tang et al. 2019), the model with
 153 425,223 grids is adopted.



154

155

(a) Axial distribution of pressure



156

157

158

(b) Radial distribution of velocity

Fig. 3 Grid independence verification

159 2.5. Experimental verification

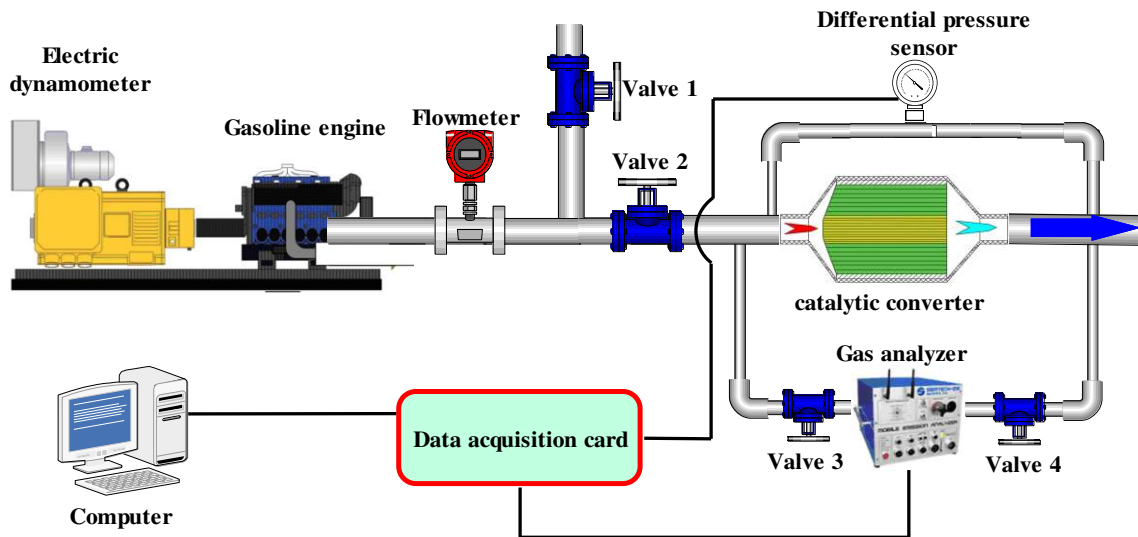
160 To further verify the accuracy of the improved model, a bench test is conducted, as shown in Fig. 4.

161 The operating parameters of the gasoline engine in the experiment are shown in Table 4. The experimental
 162 ambient temperature is 288~293 K and the ambient pressure is 101.23 kPa.

163 **Table. 4** Operation parameters of gasoline engine

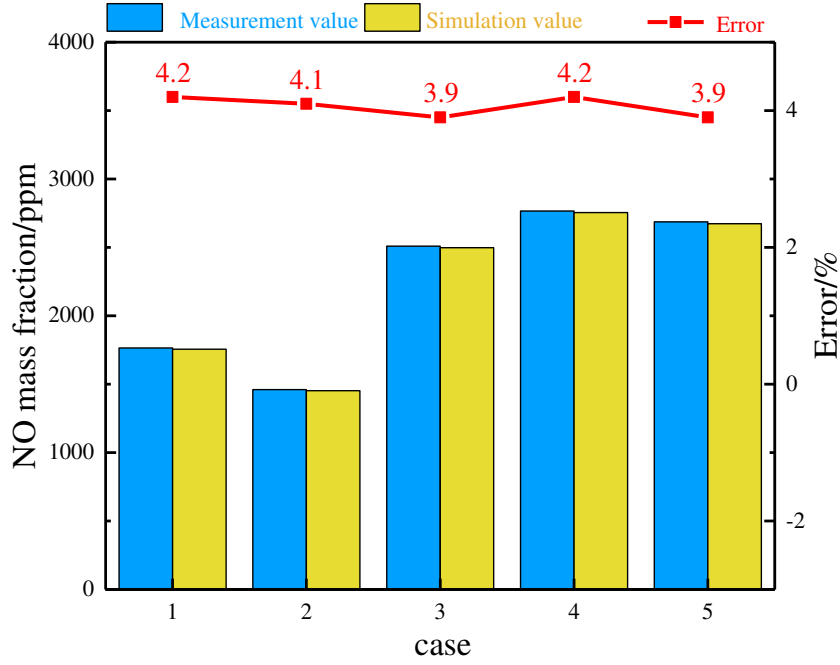
Cases	Speed($r \cdot \text{min}^{-1}$)	Torque(Nm)	Power(kW)	Fuel consumption($\text{kg} \cdot \text{h}^{-1}$)	Excess air Ratio
1	2500	41.5	10.85	3.08	1.0086
2	2500	30.4	7.95	2.52	1.0075
3	2500	19.7	5.16	2.15	1.0213
4	2500	15.6	4.09	1.89	1.0326
5	2500	10.2	2.68	1.63	1.0711

164 **Fig. 4** Schematic of the experimental apparatus



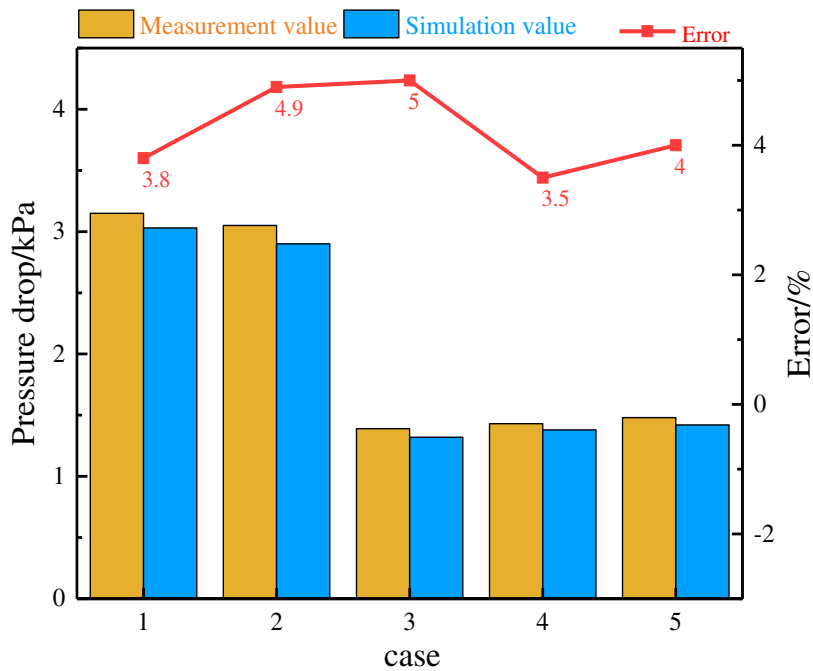
165 **Fig. 5** shows the comparison between experimental values and simulated values under different
 166 working conditions. It can be found that the measured results of NO and pressure drop are in good
 167 agreement with the simulated results, and the maximum relative errors are both less than 5%. Factors
 168 contributing to the error include: (1) The simulation model assumes that the flow in each group of exhaust

169 ducts is uniform, while the actual flow in each group of exhaust ducts is not completely uniform; (2)
 170 Experimental measurement error. Therefore, all the cases are considered as good calibration and provide a
 171 basis for further research.



172
 173

(a) NO mass fraction and error



174
 175
 176
 177

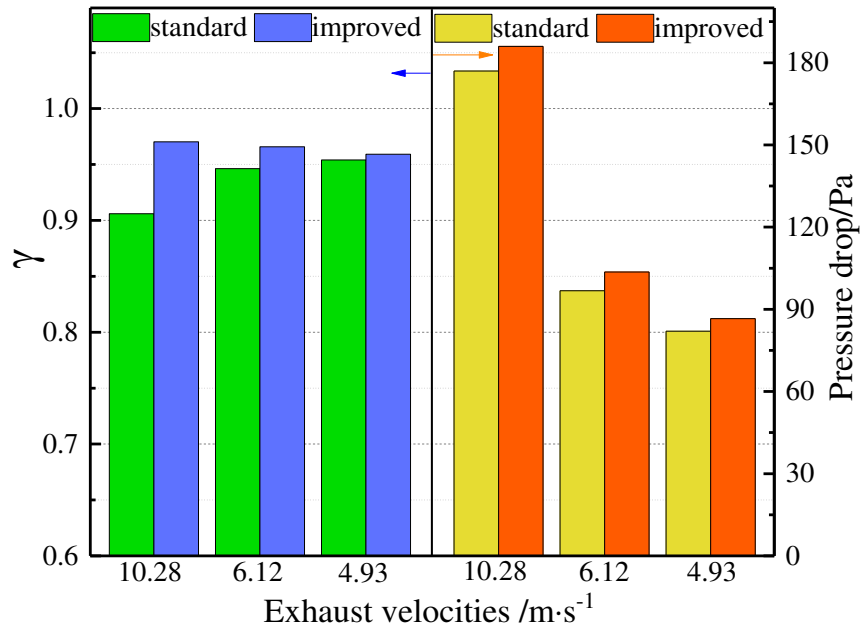
(b) Pressure drop and error

Fig. 5 Catalytic converter outlet NO mass fraction and pressure drop

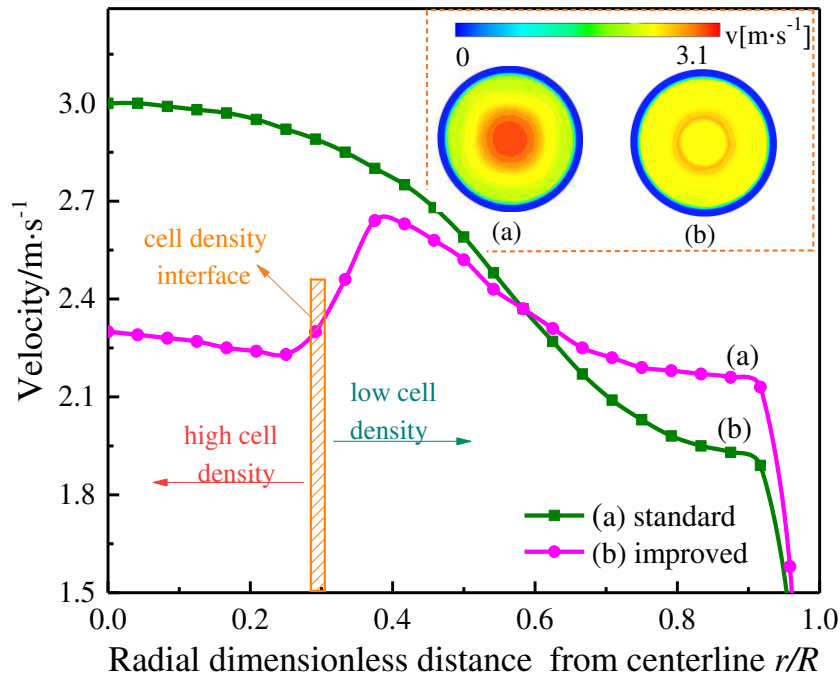
178 2.6. Performance comparative analysis

179 To demonstrate the flow characteristics and purification performance of the improved catalytic
180 converter, the gas uniformity, carrier pressure drop and NO conversion rate of the standard and improved
181 catalytic converters are compared. The carrier cell density of the standard catalytic converter is 400 cpsi,
182 and other geometrical parameters are the same.

183 As can be found from **Fig. 6(a)**, the γ and carrier pressure drop of the improved catalytic converter are
184 higher than those of the standard catalytic converter. Under the exhaust inlet velocity of $10.28 \text{ m}\cdot\text{s}^{-1}$, the γ
185 of the improved and standard catalytic converters are 0.9703 and 0.9060, and the pressure drop is 177 Pa
186 and 189 Pa respectively. The γ and p increased by 0.0643 and 6.78% respectively. **Fig. 6(b)** exhibits the
187 radial distribution of the velocities. Obviously, the velocities of the standard catalytic converter decrease
188 and change greatly along radius. The velocities of improved catalytic converter have a trend of decreasing
189 gradually at first then increasing and finally decreasing along radius, and change small. This phenomenon
190 is explained as follows. For standard catalytic converters, the exhaust mainly concentrates in the carrier
191 middle and flows less to the edge under the influence of inertia. For improved catalytic converters, the
192 resistance of the high cell density carrier is greater than that of the low cell density carrier, and the tapered
193 end face acts as a guide to the exhaust, making more exhaust flow to the edge with less resistance. Therefore,
194 the γ of improved catalytic converters is higher. As the resistance of the high cell density carrier is large and
195 the carrier has a tapered end face, which increases the resistance and leads to the increase of the carrier
196 pressure drop of the improved catalytic converter, but the increase is small.



(a) Carrier pressure drop and gas uniformity under three cases



(b) Radial distribution of velocities at the carrier outlet

Fig. 6 Comparison of gas uniformity and carrier pressure drop

197

198

199

200

201

202

203

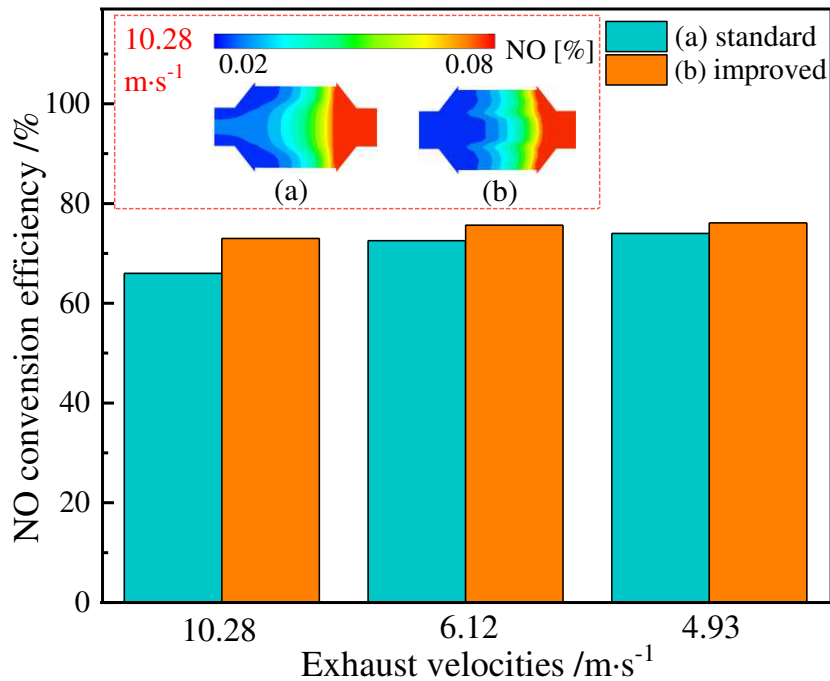
204

205

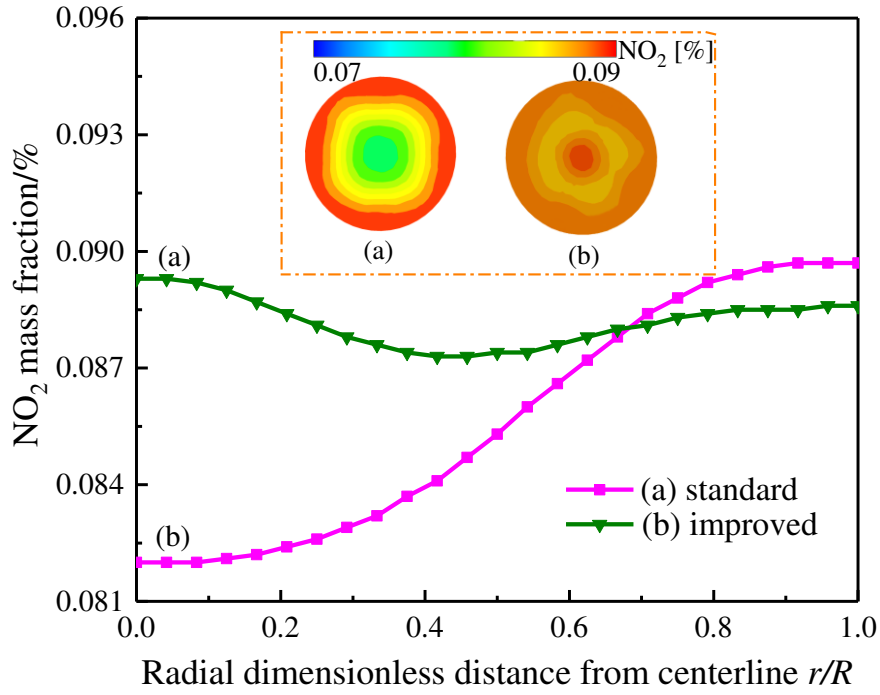
According to **Fig. 7(a)**, the NO conversion rates of the improved catalytic converter are all higher than that of the standard catalytic converter. Under the exhaust inlet velocity of $10.28 \text{ m}\cdot\text{s}^{-1}$, the NO conversion rate of the improved catalytic converters is 73.1%; compared with the traditional catalytic converter, which increases by 7.0%. **Fig. 7(b)** shows the radial distribution of NO₂ mass fraction under the exhaust inlet

206 velocity of $10.28 \text{ m}\cdot\text{s}^{-1}$. As can be found that the NO_2 mass fraction of the standard catalytic converter
 207 increases gradually along radius, and the distribution is uneven. While the NO_2 mass fraction of the
 208 improved catalytic converter tends to decrease first and then increase, and the distribution is more uniform.
 209 This phenomenon is attributed to the following reasons. The contact probability and contact time of NO
 210 with catalyst decrease with the increase of velocity, resulting in the lower NO_2 mass fraction. The velocity
 211 of standard catalytic converter decreases along the radial direction and changes greatly, which leads to the
 212 gradual increase of NO_2 mass fraction and the difference is large. However, the improved catalytic converter
 213 has lower velocity and larger specific surface area, which makes NO catalysis more sufficient, leading to a
 214 higher NO_2 mass fraction and more uniform distribution. Therefore, the NO conversion rate of the improved
 215 catalytic converter is higher.

216 In summary, the improved catalytic converter can effectively improve the flow characteristics and
 217 purification performance, the increase of pressure drop is not large, so it is an ideal catalytic converter.



(a) NO conversion rates under three cases



(b) Radial distribution of NO₂ mass fraction at exit

Fig. 7 Comparison of NO conversion rate and NO₂ mass fraction

3. Results and discussion

To design a more ideal tapered variable cell density carrier catalytic converter, the effect of structural parameters on its performance must be discussed. Compared with the standard carrier structure, the improved catalytic converter is mainly changed in the carrier inlet end face and the carrier density. Therefore, this work focuses on exploring the influence rules of cell density combination, tapered height, high cell density radius and tapered end face radius.

3.1. Influence of cell density combination

Keeping the other structure of the improved catalytic converter unchanged, the catalytic converters with different cell density combinations are simulated under three working conditions. The parameters of cell density combination are shown in **Table 5**.

Table 5 Cell density combination parameters

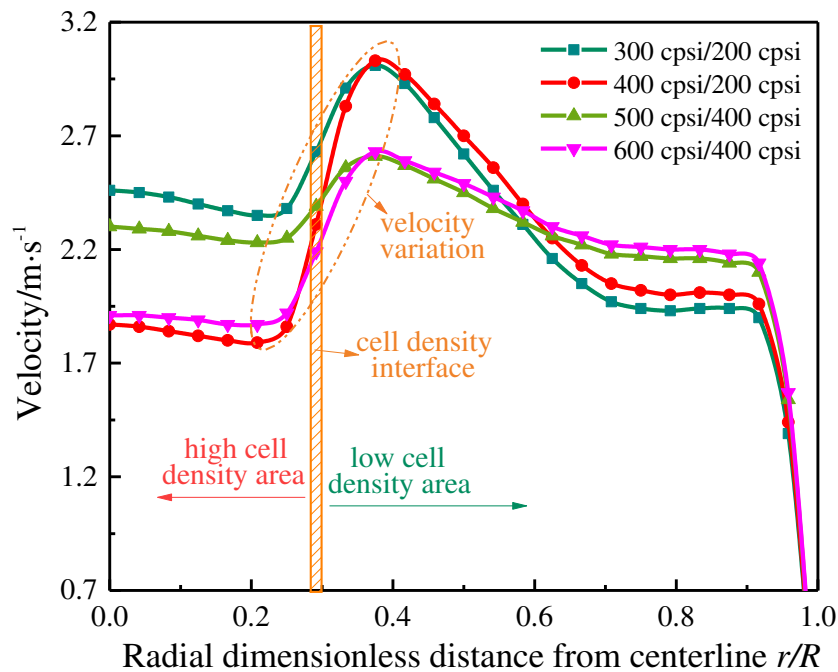
Cases	High/Low cell density(cpsi)	High/Low porosity(%)	High/Low specific surface area
-------	-----------------------------	----------------------	--------------------------------

1	300/200	78/82	2411/2021
2	400/200	85/82	2728/2021
3	400/300	85/78	2728/2411
4	500/300	72/78	2995/2411
5	500/400	72/75	2995/2728
6	600/400	70/75	3236/2728
7	600/500	70/72	2728/2411
8	700/500	67.7/72	3429/2995
9	700/600	67.7/70	3429/3236

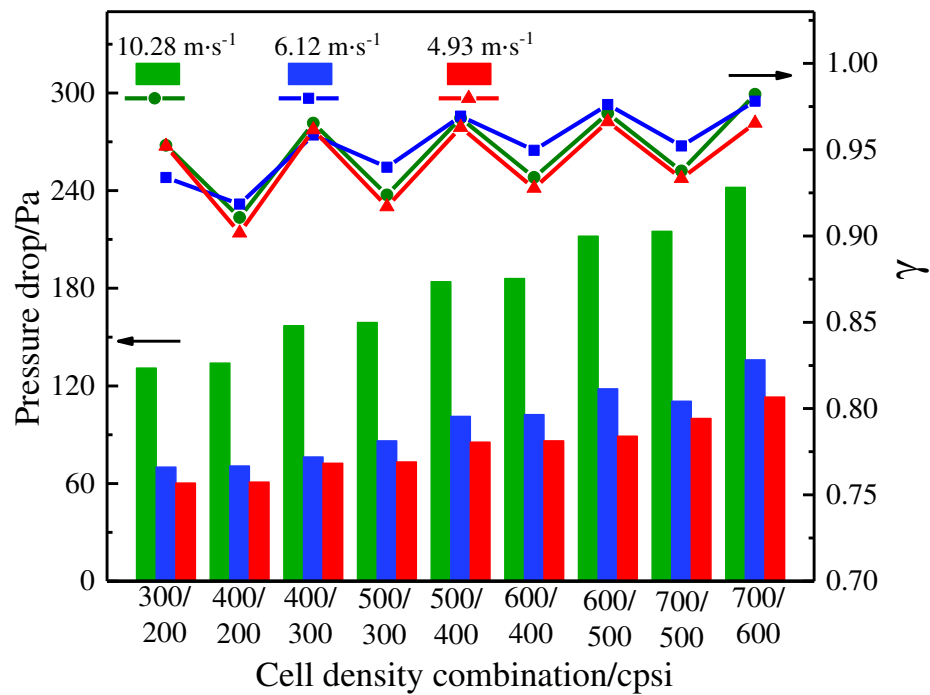
234 **Fig. 8(a)** shows the influence of different cell density combinations on the carrier outlet velocity under
235 the exhaust inlet velocity of $10.28 \text{ m}\cdot\text{s}^{-1}$. As can be found, with the increase of radius, the velocities decrease
236 gradually at first, then increases rapidly near the cell density interface, and then decreases again. The major
237 reason is that most of the exhaust flows along the axial direction and less along the radial direction due to
238 the influence of inertia, resulting in the velocity decreases along the radius. However, the carrier resistance
239 suddenly decreases at the cell density interface, resulting in the velocity increase rapidly. It can also be
240 found that when the high and low cell densities are different, the larger the cell density combination, the
241 smaller the velocity variation near the cell density interface. 500 cpsi/400 cpsi is higher than 400 cpsi/200
242 cpsi, but the velocity variation of 500 cpsi/400 cpsi is smaller than that of 400 cpsi/200 cpsi. Besides, when
243 the low cell density is the same, the velocity variation enhances with the high cell density increases. Under
244 the low cell density is 400 cpsi, the high cell density increases from 500 cpsi to 600 cpsi, the velocity
245 variation greatly. The reason is that as the cell density combination is large, the resistances of high and low
246 cell density are both high, which makes the relative resistance difference smaller, resulting in a small
247 velocity variation. When the low cell density is the same, the larger the high cell density, the greater the

248 resistance difference, which leads to the bigger velocity variation.

249 It can be found from **Fig. 8(b)** that with the increase of cell density combination, γ shows a cyclic
250 change of decreasing first and then increasing. When the high and low cell densities are different, γ increases
251 gradually with the increase of cell density combination. The cell density of 700 cpsi/600 cpsi is the highest,
252 and its γ reaches the highest, which is 0.9821 at the exhaust inlet velocity of 10.28 m·s⁻¹. The main reason
253 is that the higher the carrier cell density, the greater the resistance of carrier, which makes more exhaust
254 flow to the edge and distributes more evenly. However, when the low cell density of cell density
255 combination is the same, the smaller the high cell density, the better the gas uniformity. When the low cell
256 density is 500 cpsi, γ decreases from 0.9710 to 0.9377 when the high cell density increases from 600 cpsi
257 to 700 cpsi. This is because when the low cell density is the same, the higher the high cell density, the greater
258 the resistance difference, which leads to the great variation of velocity at the cell density interface and
259 reduces the uniformity.



260
261 (a) Radial distribution of carrier outlet velocity



(b) Carrier pressure drop and gas uniformity

Fig. 8 Gas uniformity and carrier pressure drop

262

263

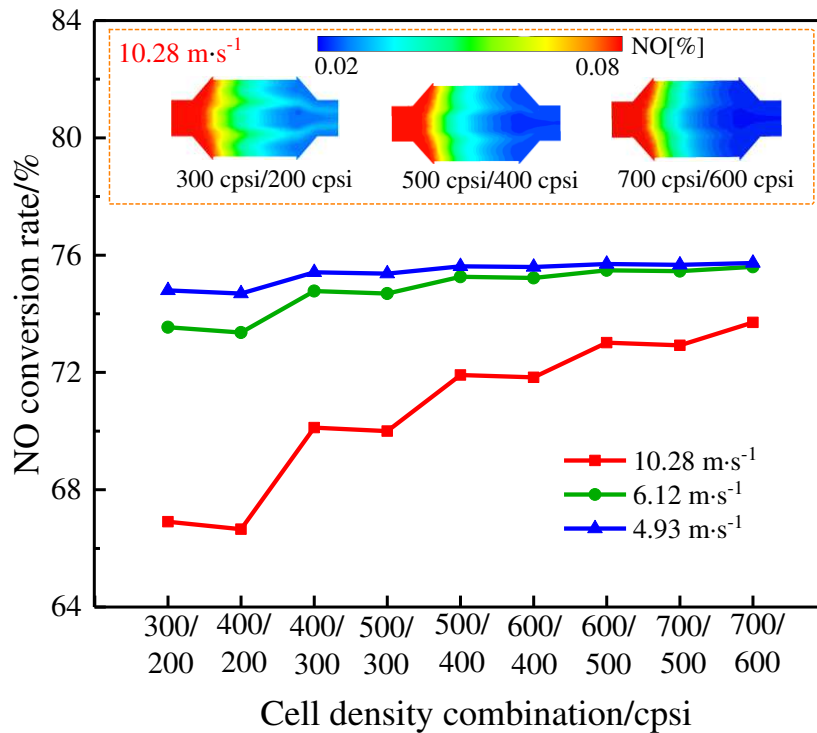
264

265 It is clear from **Fig. 8(b)** that the larger the cell density combination, the greater the carrier pressure
 266 drop. When the cell density is 700 cpsi/600 cpsi, the carrier pressure drop reached the maximum value of
 267 232 Pa. The reason is that the higher the cell density, the greater the resistance along the path, so that the
 268 carrier pressure drop increases.

269 **Fig. 9(a)** shows the influence of different cell density combinations on NO conversion rate under three
 270 cases. It can be found that with the increase of cell density combination, NO conversion rate shows a cyclic
 271 change of decreasing first and then increasing. When the high and low cell densities of cell density
 272 combination are different, NO conversion rate increases with the cell density combination enhance. When
 273 the cell density increases from 400 cpsi/200 cpsi to 700 cpsi/600 cpsi, NO conversion rate increases from
 274 66.6% to 73.7% under the exhaust inlet velocity of 10.28 m·s⁻¹. The reason is that the greater the cell density
 275 combination, the larger the specific surface area of the carrier and the smaller the velocity, which increases
 276 the contact probability and time between NO and catalyst, leads to NO conversion rate increase. However,

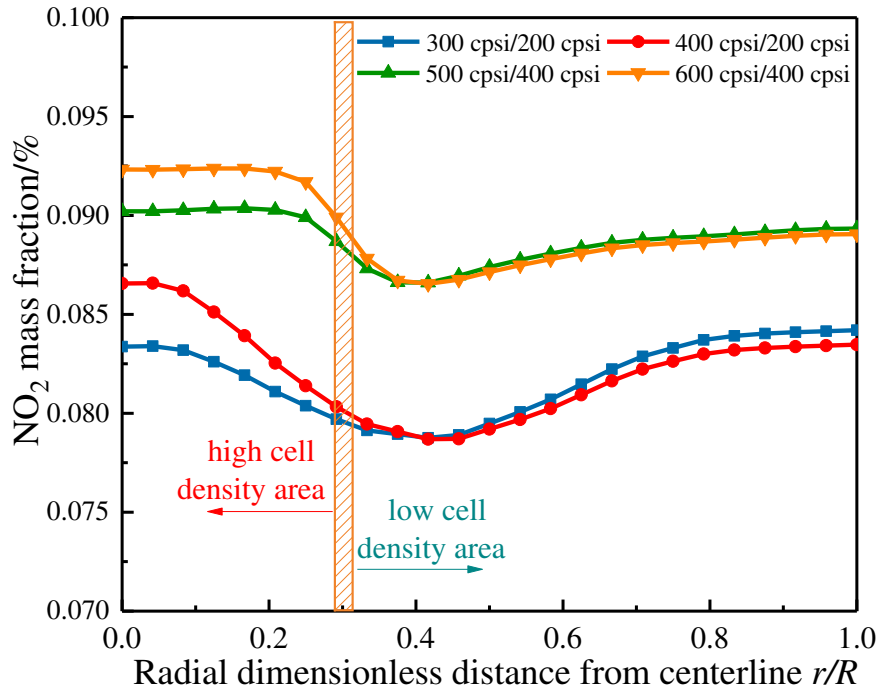
277 when the low cell density of cell density combination is the same, NO conversion rate decreases with the
 278 high cell density increases. Under the low density is the same as 200 cpsi, when the high cell density
 279 increased from 300 cpsi to 400 cpsi, NO conversion rate fell to 66.9% from 66.6%. This is because when
 280 the low cell density is the same, increasing the high cell density will cause more exhaust to flow through
 281 the low cell density region, which leads to the limitation of NO catalysis in the low cell density region, thus
 282 reducing NO conversion rate.

283 **Fig. 9(b)** exhibits the impact of different cell density combinations on the NO₂ mass fraction at the
 284 outlet at the exhaust inlet velocity of 10.28 m·s⁻¹. It can be found that when the high and low cell densities
 285 are different, the larger the cell density combination, the higher the NO₂ mass fraction. The NO₂ mass
 286 fraction of 600 cpsi/400 cpsi is higher than that of 400 cpsi/200 cpsi. The reason is that the larger the cell
 287 density combination, the larger the specific surface area and the lower the velocity, which makes the NO
 288 catalysis more sufficient and the NO₂ mass fraction higher.



(a) NO conversion rate

289
290



(b) Distribution of NO₂ mass fraction at export

Fig. 9 NO conversion rate and NO₂ mass fraction

291

292

293

294

295

296

297

298

299

300

301

302

303

304

305

306

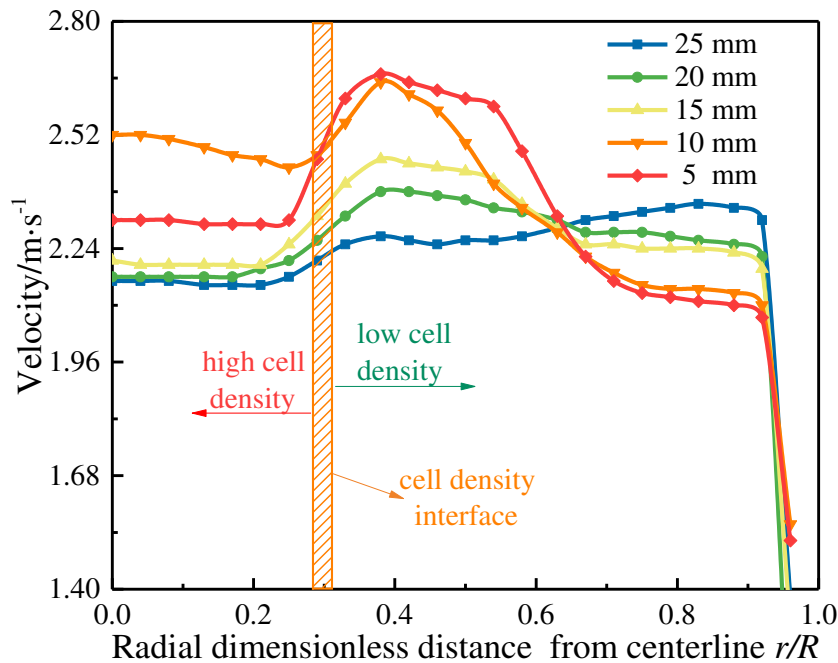
It can also be found from **Fig. 9(b)** that when the low cell density is the same, the lower the high cell density, the higher the NO₂ mass fraction in the low cell density region. Under the condition of the same low cell density of 200 cpsi, the NO₂ mass fraction of 300 cpsi/200 cpsi is higher than that of 400 cpsi/200 cpsi in low cell density region. This is because when the low cell density is the same, the higher the high cell density, the higher the velocity in the low cell density area, which leads to insufficient NO catalysis and thus lowers the NO₂ mass fraction. Therefore, it is beneficial to improve the performance of catalytic converters by appropriately increasing the cell density combination and decreasing the high cell density.

3.2. Influence of tapered height

Fig. 10(a) shows the influence of different tapered heights on the radial distribution of the velocity at the carrier outlet when the exhaust inlet velocity of 10.28 m·s⁻¹. As can be found, when the tapered height is lower than 20 mm, the velocity exhibits a trend of gradually decreasing first, then increasing near the cell density interface, and then decreasing gradually. However, when the tapered height is greater than 25 mm, the velocity increase gradually. The main reason is that when the tapered height is lower than 20 mm, the

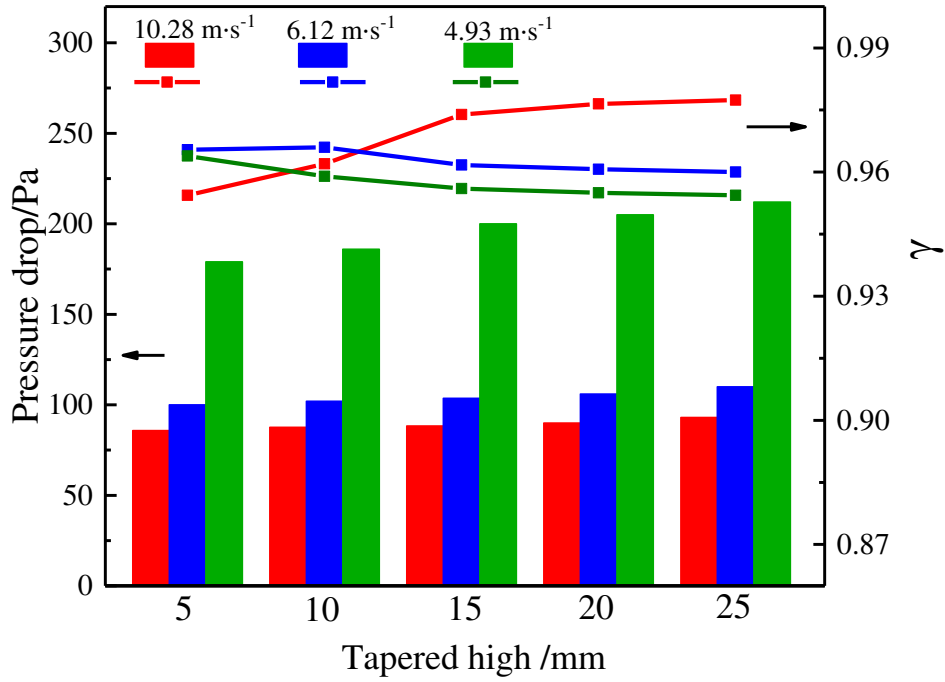
307 velocity decreases gradually along the radial due to the influence of inertia, and the carrier resistance
 308 decreases suddenly at the cell density interface, leading to its increase rapidly. The conductivity increases
 309 with the tapered height enhances, and when the tapered height is higher than 25 mm, more exhaust is
 310 diverted to the edge of the carrier, resulting in a gradual increase in velocity.

311 **Fig. 10(b)** shows the influence of tapered height on gas uniformity and pressure drop under three cases.
 312 It can be found that γ increases gradually with the tapered height enhance under the exhaust inlet velocity
 313 of $10.28 \text{ m}\cdot\text{s}^{-1}$. γ increases from 0.9544 to 0.9774 when the tapered height enhances from 5 mm to 25 mm.
 314 The main reason is that when the exhaust inlet velocity is $10.28 \text{ m}\cdot\text{s}^{-1}$, the higher the tapered height, the
 315 greater the flow conductivity, so that more exhaust is diverted to the low cell density region, which improves
 316 the velocity in the low cell density region and the gas uniformity. However, when the exhaust inlet velocity
 317 is $6.12 \text{ m}\cdot\text{s}^{-1}$ and $4.93 \text{ m}\cdot\text{s}^{-1}$, γ decreases with the increase of tapered height. The main reason is that the
 318 kinetic energy of exhaust is small, and it is easy to change the flow direction due to the guide surface, which
 319 makes the velocity in the low cell density region too high, leads to the decrease of gas uniformity.



(a) Radial distribution of velocity at carrier exit

320
 321



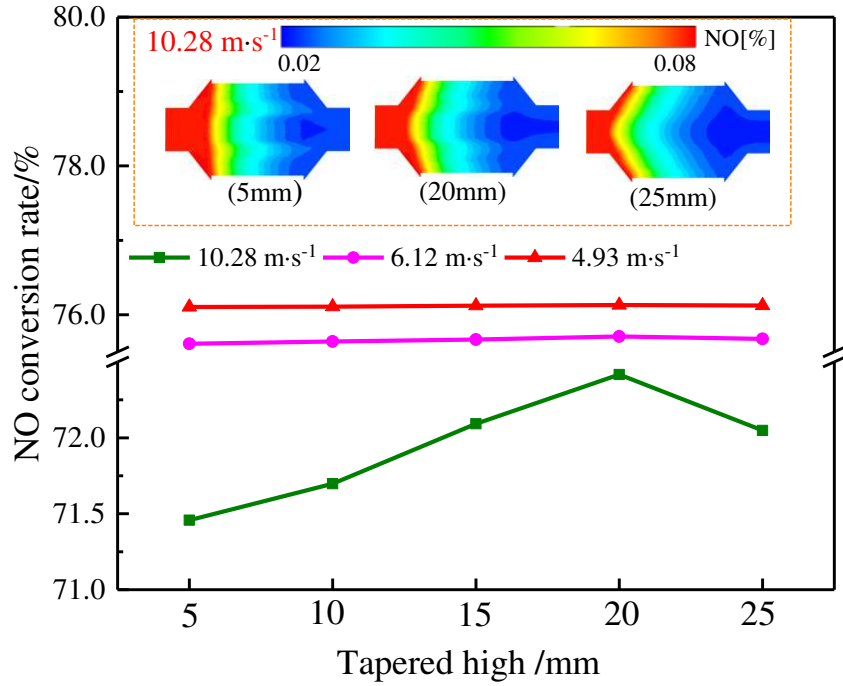
(b) Gas uniformity and carrier pressure drop

Fig. 10 Gas uniformity and carrier pressure drop

From **Fig. 10(b)**, It can be found that the carrier pressure drop increases with the increase of tapered height. The carrier pressure drop increases from 179 Pa to 212 Pa when the tapered height enhances from 5 mm to 25 mm at the exhaust inlet velocity of 10.28 m·s⁻¹. This is because the higher the tapered height, the larger the total carrier length, which increases the flow resistance.

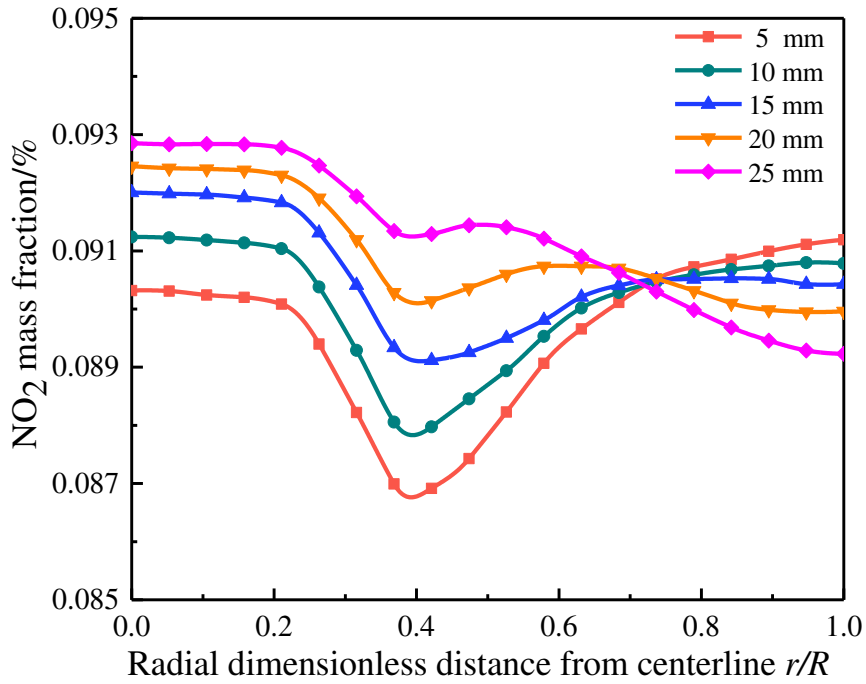
Fig. 11(a) exhibits the influence of tapered height on NO conversion rate under three cases. As can be found, NO conversion rate shows a trend of gradually increasing and then decreasing with the increase of the tapered height at the exhaust inlet velocity of 10.28 m·s⁻¹. As the tapered height increases from 5 mm to 25 mm, NO conversion rate increases from 71.4% to 72.4% and then decreases to 72.0%, and reaches the maximum at 20 mm. The chief reason is that when the tapered height increases, the total reaction surface area of the support increases and the velocity decreases, which makes the contact probability and time between NO and catalyst increase, and leads to the NO conversion rate increases. However, when the tapered height is greater than 20 mm, more exhaust is diverted to the low cell density area, and the velocity is high, which restricts the NO catalytic activity and decreases the NO conversion rate. It can also be found

338 from **Fig. 11(a)** that the tapered height has little impact on the NO conversion rate when the exhaust inlet
 339 velocity is $6.12 \text{ m}\cdot\text{s}^{-1}$ and $4.93 \text{ m}\cdot\text{s}^{-1}$. This is because when the exhaust velocity is low, the contact
 340 probability and contact time between NO and catalyst are sufficient, and NO catalysis is mainly affected by
 341 temperature, which makes the change of tapered height have little impact on NO conversion rate.



342
343

(a) NO conversion rate



344
345
346

(b) Radial distribution of NO₂ mass fraction at carrier outlet

Fig. 11 NO conversion rate and NO₂ mass fraction

347 **Fig. 11(b)** shows the influence of different tapered heights on the radial distribution of NO₂ mass
348 fraction at the outlet at the exhaust inlet velocity of 10.28 m·s⁻¹. It can be found that when the tapered heights
349 are less than 15 mm, the NO₂ mass fraction decreases and then increases along the radial direction of the
350 outlet. However, when the tapered heights are higher than 20 mm, the NO₂ mass fraction decreases, then
351 increases and finally decreases. The reason is that when the tapered height is less than 15 mm, the velocity
352 increases rapidly near the cell density interface and then decreases gradually, which makes the contact
353 probability and contact time between NO and catalyst decrease gradually and then increase gradually,
354 resulting in the NO₂ mass fraction decreasing first and then increasing gradually. However, as the tapered
355 height is higher than 20 mm, more exhaust is guided to the edge, which leads to the limitation of NO
356 catalysis in the edge area and the lower NO₂ mass fraction.

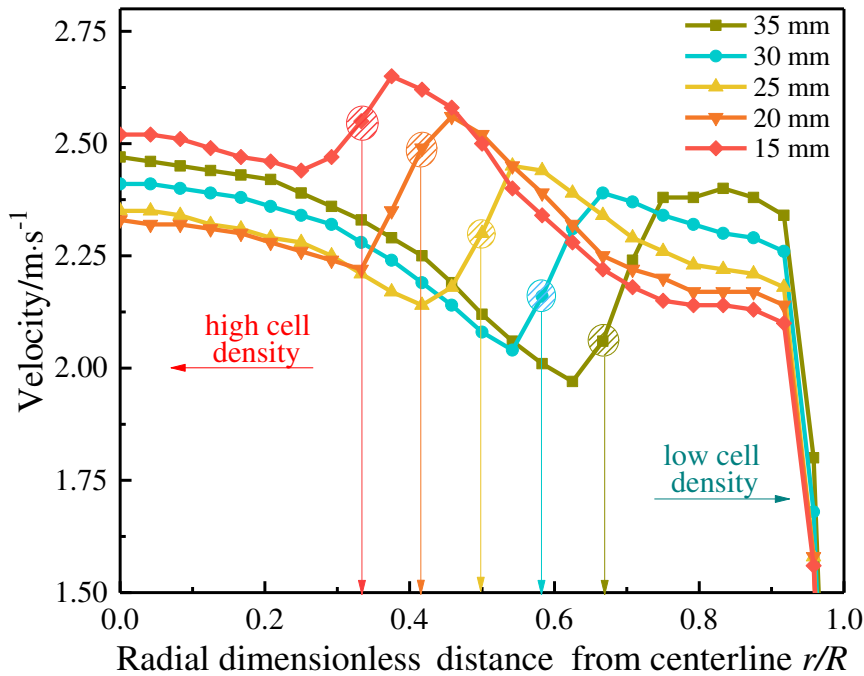
357 3.3. Influence of high cell density radius

358 **Fig. 12(a)** shows the influence of high cell density radius on the radial distribution of carrier outlet
359 velocity at the exhaust inlet velocity of 10.28 m·s⁻¹. As shown in **Fig. 12(a)**, the exhaust velocity shows a
360 trend of first gradually decreasing, then increasing and finally decreasing along the radius. The reason is the
361 same as the explanation of **Fig. 8(a)**. It can be found that the velocity at the edge increases as the high cell
362 density radius increases. The maximum velocity at the edge increases from 2.1 m·s⁻¹ to 2.4 m·s⁻¹ as the high
363 cell density radius enhances from 15 mm to 35 mm. This is because the larger the high cell density radius,
364 the more exhaust flows to the low cell density area with less resistance, and the velocity increases. Therefore,
365 the velocity at the edge should be appropriately reduced as the high cell density radius is 25 mm

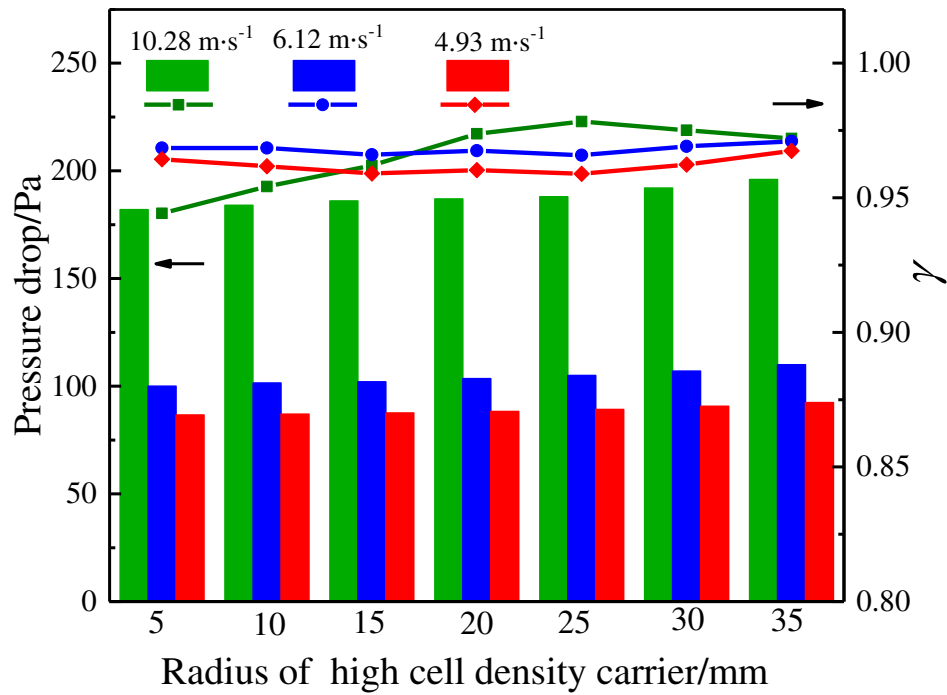
366 **Fig. 12(b)** shows the influence of high cell density radius on gas uniformity and carrier pressure drop
367 under three cases. It can be found that γ increases at first and then decreases with the increase of high cell
368 density radius at the exhaust inlet velocity of 10.28 m·s⁻¹. As the high cell density radius enhances from 5
369 mm to 35 mm, γ increases from 0.9442 to 0.9783 and then decreases to 0.9720, and reaches the maximum

370 at 25 mm. The reason is that when the high cell density radius area is small, the velocity of the low cell
 371 density area changes greatly. On the contrary, the velocity changes greatly in the region with high cell
 372 density, thus reducing the flow field uniformity. It can also be found that the closer the high cell density
 373 radius is to 25 mm, the lower the γ under the exhaust inlet velocity of $6.12 \text{ m}\cdot\text{s}^{-1}$ and $4.93 \text{ m}\cdot\text{s}^{-1}$. The reason
 374 is that the kinetic energy of exhaust is small and the velocity is easily disturbed. When the high cell density
 375 radius is 25 mm, the change of velocity caused by the change of cell density has a large influence range,
 376 thus reducing the uniformity.

377 It can also be found from **Fig. 12(b)** that the carrier pressure drop increases with the high cell density
 378 radius enhance. The carrier pressure drop increases from 182 Pa to 198 Pa as the high cell density radius
 379 increases from 5 mm to 25 mm under the exhaust inlet velocity of $10.28 \text{ m}\cdot\text{s}^{-1}$. This is because the larger
 380 the high cell density radius, the greater the resistance of the carrier along the path, which increases the
 381 pressure drop.



(a) Radial distribution of velocity at carrier exit



(b) Gas uniformity and carrier pressure drop

Fig. 12 Gas uniformity and carrier pressure drop

384

385

386

387

388

389

390

391

392

393

394

395

396

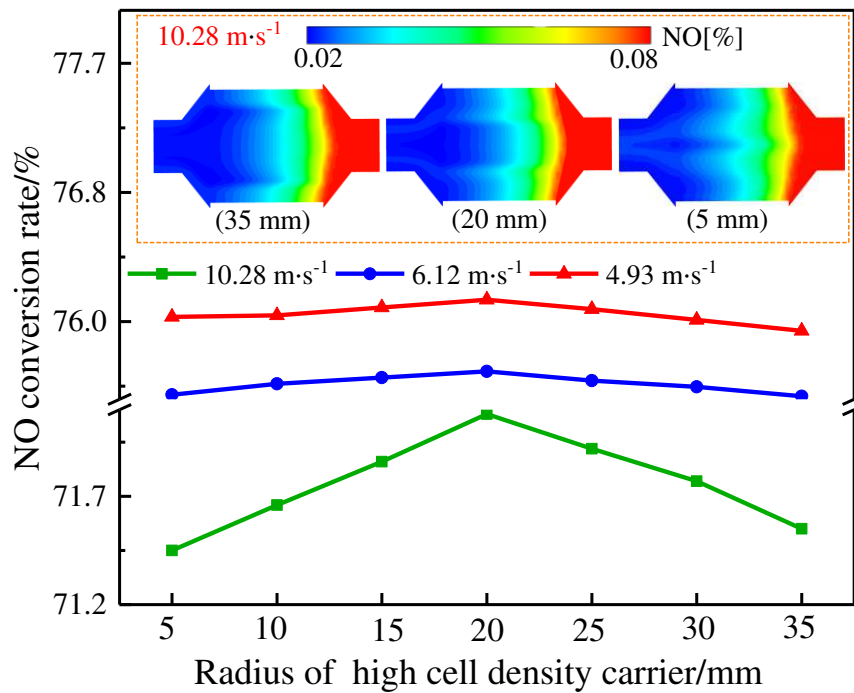
397

398

The influence of high cell density radius on NO conversion rate under three cases is shown in Fig. 13(a). As can be found, NO conversion rate increases first and then decreases with the high cell density radius increase. NO conversion rate increases from 71.4% to 72.1% and then decreases to 71.5% as the high cell density radius enhances from 5 mm to 35 mm at the inlet velocity of 10.28 m·s⁻¹, and reaches the maximum value at 20 mm. This issue is explained as follows. When the high cell density radius is small, the velocity is large in the region of high cell density and near the cell density interface, which restricts NO catalysis in this region. However, when the high cell density radius is larger, the velocity is larger in the area of low cell density, which leads to insufficient NO catalysis in this area, thus reducing the NO conversion rate. The velocity is more uniform when the high cell density radius is 20 mm, and the overall catalysis of NO is more sufficient.

Fig. 13(b) shows the influence of different high cell density radius on the radial distribution of NO₂ at the outlet under the exhaust inlet velocity of 10.28 m·s⁻¹. It is obvious that when the high cell density radius

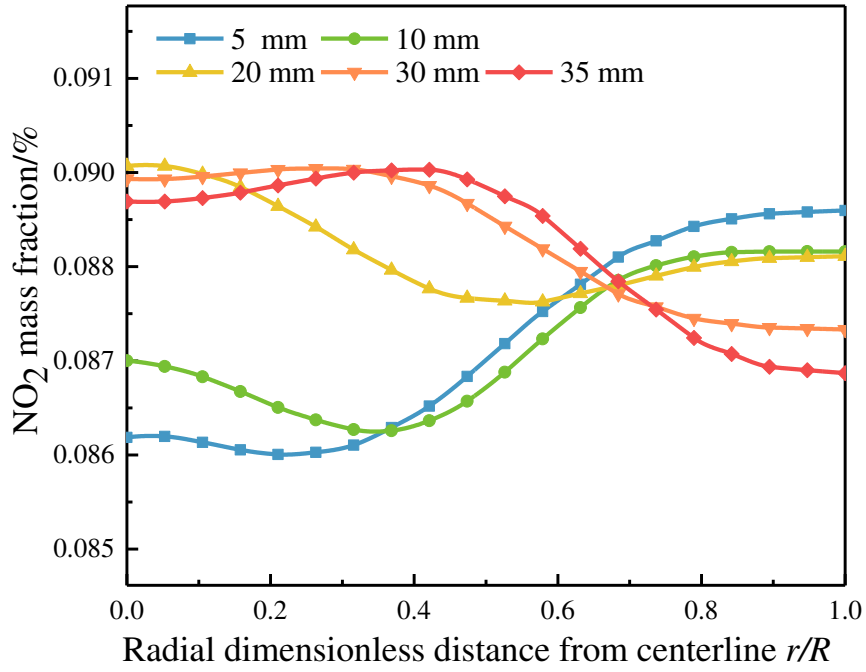
399 is less than 10 mm, the NO₂ mass fraction exhibits a trend of gradually decreasing and then increasing,
 400 which is small in the area of dimensionless radius from 0 to 0.65. However, when the high cell density
 401 radius is greater than 30 mm, the NO₂ mass fraction shows a trend of gradually increasing and then
 402 decreasing, and it is small in the area of dimensionless radius from 0.65 to 1. This phenomenon is explained
 403 for the following reasons. When the high cell density radius is small, the velocity is large in the region of
 404 high cell density and the cell density interface, which makes the NO₂ mass fraction small in the region of
 405 dimensionless radius from 0 to 0.65. However, when the high cell density radius is larger, the velocity is
 406 larger in the region of low cell density, resulting in a lower NO₂ mass fraction in the region from 0.65 to 1.
 407 The radial distribution of NO₂ mass fraction is higher, and more uniform when the high cell density radius
 408 is 20 mm, and the NO conversion rate is higher. Therefore, the high cell density radius of 20 mm is selected, the NO
 409 conversion rate is the highest, the gas uniformity is higher.



410

411

(a) NO conversion rate



(b) Radial distribution of NO₂ mass fraction at the outlet

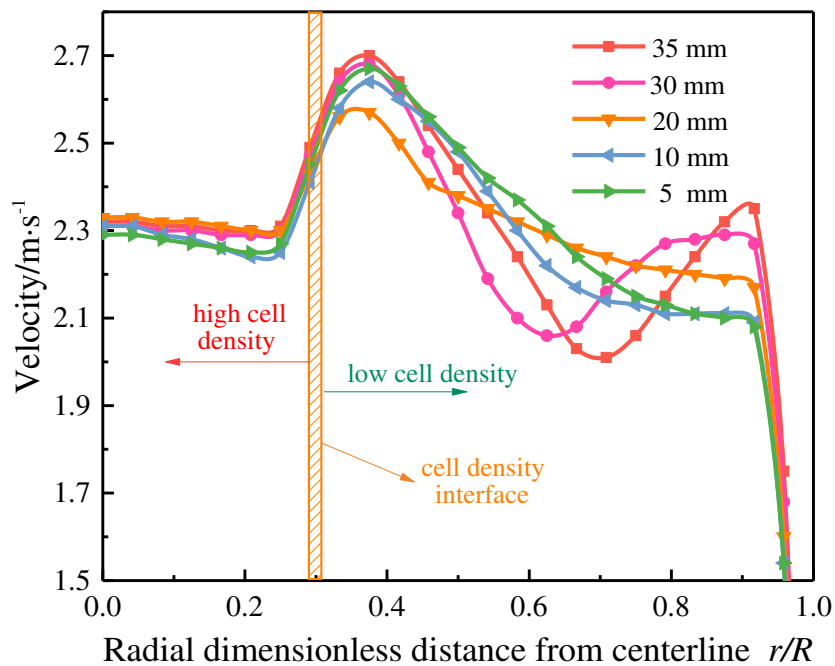
Fig. 13 NO conversion rate and NO₂ mass fraction

3.4. Influence of tapered end face radius

Fig. 14(a) shows the influence of different tapered end face radius on the radial distribution of the velocity at carrier outlet under the exhaust inlet velocity of 10.28 m·s⁻¹. It is obvious that, when the tapered end face radius is greater than 30 mm, the velocity in the low cell density area decreases first and then increases, and the change is large. However, when the tapered end face radius is less than 10 mm, the velocity decreases and the change is larger, which is smaller at the edge. This phenomenon is mainly caused by the following reasons. The larger the tapered end face radius, the closer the conduction position of the tapered to the edge and the greater the conduction capacity. When the tapered end face radius is 30 mm (the dimensionless radius is 0.6), the conductivity of the tapered surface is strong, which makes the velocity of the area after the dimensionless radius 0.6 increase rapidly and the change gradient is large. When the tapered end face radius is 10 mm (the dimensionless radius is 0.2), the conductivity of the tapered surface is weak, so that the velocity decreases gradually after the dimensionless radius is 0.2, and it is low at the

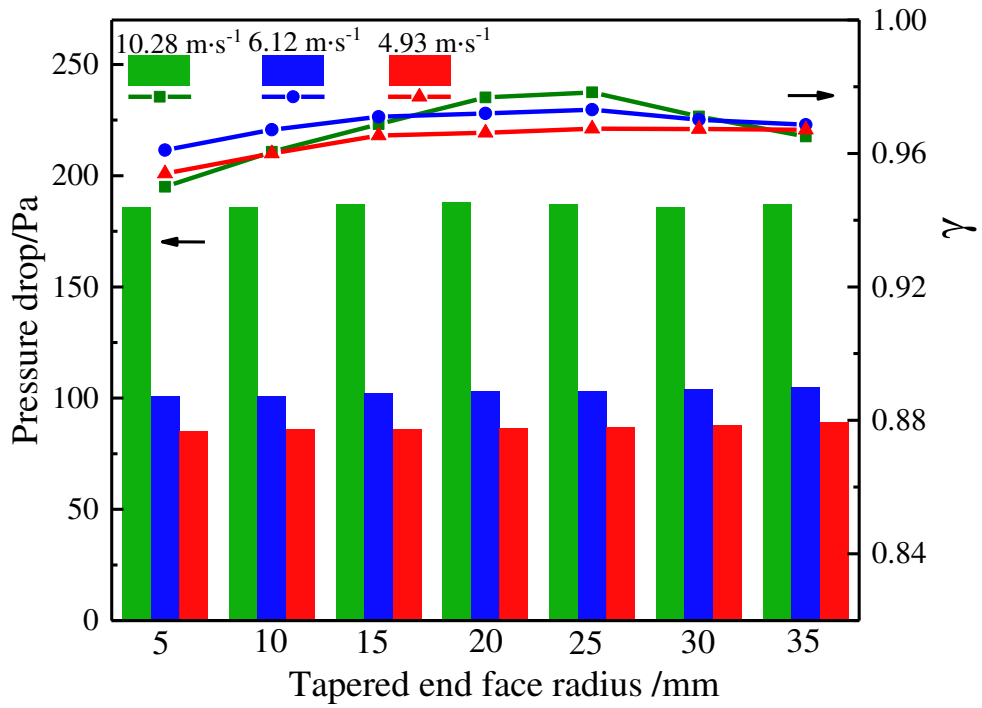
427 edge. When the tapered end face radius is 25 mm, the diversion intensity is moderate and the velocity
 428 distribution is uniform.

429 The influence of tapered end face radius on gas uniformity and carrier pressure drop under three cases
 430 is shown in **Fig. 14(b)**. It is obvious that γ increases first and then decreases with the tapered end face radius
 431 increases. When the exhaust inlet velocity is $10.28 \text{ m}\cdot\text{s}^{-1}$, γ increased from 0.9500 to 0.9784 and then
 432 decreased to 0.9651 as the tapered end face radius increased from 5 mm to 35 mm, and reached the
 433 maximum at 25 mm. The main reason is illustrated by **Fig. 14(a)**: When the tapered end face radius is large,
 434 the velocity increases first and then decreases in the low cell density region, which changes greatly; When
 435 the tapered end face radius is small, the velocity at the edge is small, thus affecting the gas uniformity. The
 436 velocity distribution is more uniform when the tapered end face radius is about 25 mm. As can be found
 437 from **Fig. 14(b)**, the carrier pressure drop gradually increases with the tapered end face radius increases,
 438 but the influence is small. The carrier pressure drop increases from 186 Pa to 189 Pa when the tapered end
 439 face radius increases from 5 mm to 35 mm. The main reason is that increasing the tapered end face radius
 440 will increase a small part of the carrier, but the flow through the area with high cell density and the area
 441 with low cell density is basically unchanged, leading to the resistance being basically unchanged.



(a) Radial distribution of velocity at carrier exit

442
 443



(b) Gas uniformity and carrier pressure drop

Fig. 14 Gas uniformity and carrier pressure drop

444

445

446

447

448

449

450

451

452

453

454

455

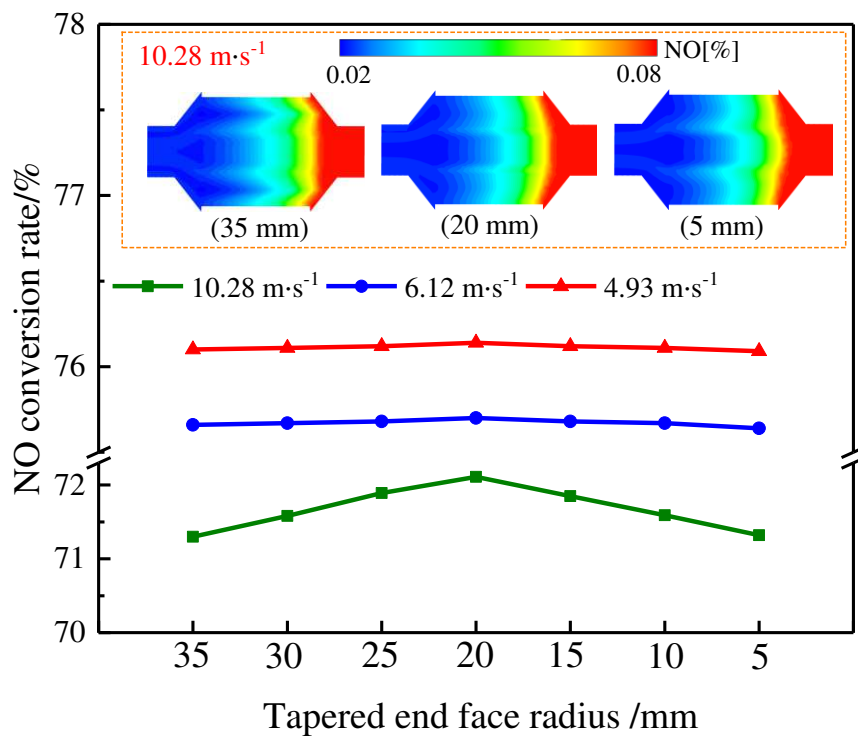
456

457

458

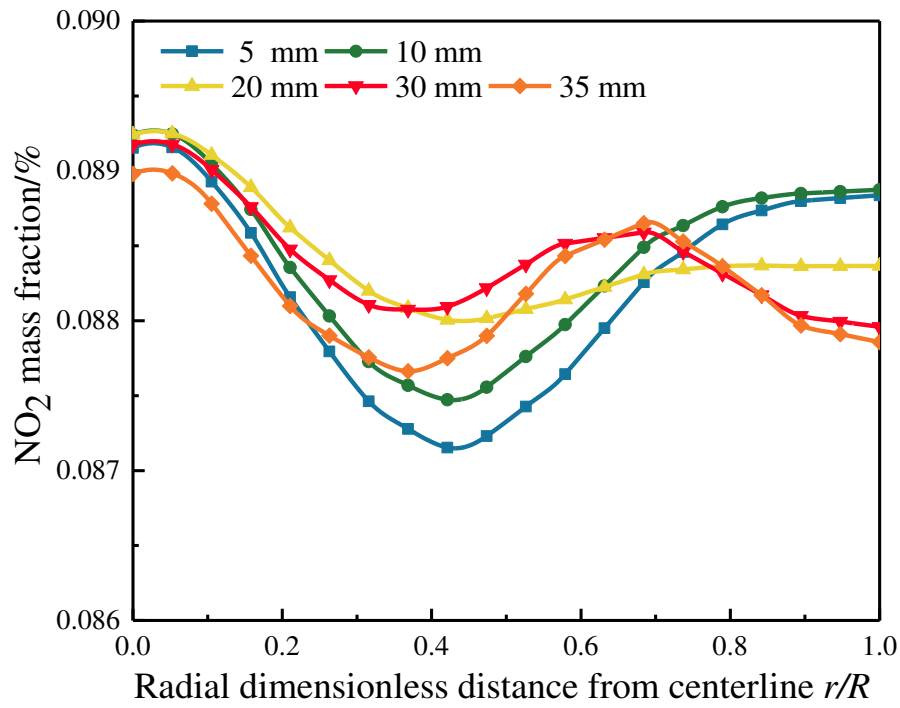
The effect of different tapered end face radius on NO conversion rate is shown in **Fig. 15 (a)**. It can be found, NO conversion rate first increases and then decreases with the tapered end face radius increases. NO conversion rate increases from 71.2% to 72.0%, and then decreases to 71.3% as the conical end radius increases from 5 mm to 35 mm under the exhaust inlet velocity of $10.28 \text{ m}\cdot\text{s}^{-1}$, and reaches the maximum value at 20 mm. The main reason is that when the tapered end face radius is larger, the edge velocity is larger, which makes NO cannot be effectively catalyzed, resulting in a lower NO conversion rate. When the radius of the tapered end face radius is small, the velocity is larger in the area around the dimensionless radius of 0.4, which makes NO catalysis insufficient. The velocity distribution is more uniform and NO catalysis is more sufficient when the tapered end face radius is 20 mm. Under the condition of inlet velocity of $6.12 \text{ m}\cdot\text{s}^{-1}$ and $4.93 \text{ m}\cdot\text{s}^{-1}$, the tapered end face radius has little effect on NO conversion. The reason is the same to the explanation of **Fig. 11(a)**.

459 **Fig. 15(b)** shows the influence of different tapered end face radius on the radial distribution of NO₂
 460 mass fraction at the outlet under the exhaust inlet velocity is 10.28 m·s⁻¹. When the tapered end face radius
 461 is less than 10 mm, the NO₂ mass fraction decreases first and then increases along the radius, and it is lower
 462 in the area near the dimensionless radius of 0.4. When the tapered end face radius is larger than 30 mm, it
 463 decreases first, then increases and finally decreases, and it is relatively low in the area of the dimensionless
 464 radius from 0.7 to 1. This is because when the tapered end face radius is small, the velocity is larger in the
 465 dimensionless region around 0.4, and when the tapered end face radius is large, the velocity is larger in the
 466 dimensionless 0.7 to 1 region, which leads to the restriction of NO catalysis and the low NO₂ mass fraction.
 467 The velocity distribution is more uniform when the tapered end face radius is 20 mm, so that the radial
 468 distribution of NO₂ mass fraction is more uniform. Therefore, when the tapered end face radius is 20 mm,
 469 the velocity is more uniform and the NO conversion rate is higher.



470
 471

(a) NO conversion rate



(b) Radial distribution of NO₂ mass fraction at outlet

Fig. 15 NO conversion rate and NO₂ mass fraction

4. Gray correlation analysis

4.1. Experimental design and calculation

The influence degree of the above structural parameters on the catalytic converter performance is further investigated by using grey relational analysis method. According to the grey relational analysis (Zhang et al. 2017; Wang et al. 2020) low cell density (x_1), high cell density (x_2), high/low cell density ratio (x_3), tapered height (x_4), high cell density carrier radius (x_5) and tapered end face radius (x_6) are taken as the influencing factors eigenvectors. Carrier pressure drop (y_1), gas uniformity (y_2) and NO conversion rate (y_3) are taken as reference feature vectors. Under the condition of exhaust inlet temperature of 575 K and velocity of 10.28 m·s⁻¹, 10 representative experimental models are studied. And the gas uniformity, no conversion and pressure drop are analyzed. The simulation conditions and results are shown in **Table 6**.

Table 6 Simulation conditions and results

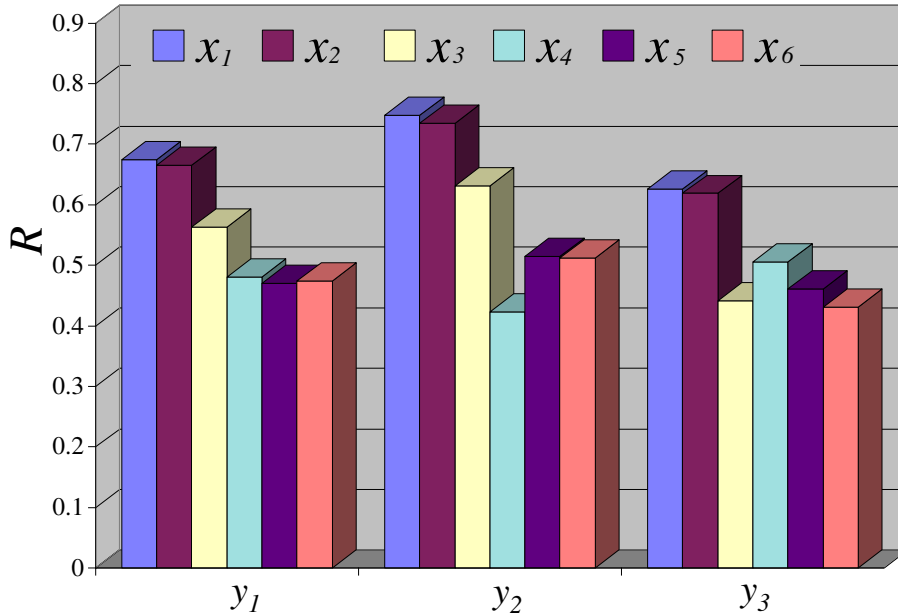
Cases	x_1 (cpsi)	x_2 (cpsi)	x_3	x_4 (mm)	x_5 (mm)	x_6 (mm)	y_1	y_2 (Pa)	y_3 (%)
-------	--------------	--------------	-------	------------	------------	------------	-------	------------	-----------

1	600	700	1.333	24	5.0	7.0	0.9794	227	82.97
2	600	700	1.333	22	7.5	9.5	0.9815	225	74.69
3	500	600	1.200	20	10.0	12.0	0.9440	219	73.03
4	500	600	1.200	18	12.5	16.0	0.9720	213	73.29
5	400	600	1.500	16	15.0	20.0	0.9707	185	72.07
6	400	600	1.500	14	17.5	22.5	0.9687	182	71.95
7	400	600	1.250	12	20.0	25.0	0.9843	180	71.93
8	400	500	1.250	10	22.5	27.5	0.9826	180	71.87
9	300	500	1.667	8	25.0	30.0	0.9659	158	69.69
10	300	500	1.667	6	27.5	32.5	0.9463	157	69.43

486 *4.2. Simulation results and analysis*

487 The influence degree of influencing factors on catalytic converter performance is expressed by the R
488 value, and the greater R is, the greater the influence is (Zuo et al. 2016; Kadier et al. 2015) According to
489 **Fig. 16**, the influence degree of each influencing factor on each reference index is as follows. For carrier
490 pressure drop: low cell density > high cell density > high/low cell density ratio > tapered height > tapered
491 end face radius > high cell density carrier radius. For gas uniformity: low cell density > high cell density >
492 high/low cell density ratio > high cell density carrier radius > tapered end face radius > tapered height. For
493 NO conversion rate: low cell density > high cell density > tapered height > high cell density carrier radius >
494 high /low cell density ratio > tapered end face radius. The low cell density is a key factor affecting the
495 improved catalytic converter. This issue is explained as follows. The low cell density determines the
496 resistance in the edge area, which affects the flow degree of the exhaust to the edge, thus affecting the gas
497 uniformity. In addition, because most of the exhaust flows through the low cell density area, the resistance
498 in the low cell density area directly affects the pressure drop of the overall carrier. Meanwhile, the low cell

499 density area becomes the main site for NO catalyzing and directly affects the overall NO conversion rate.
 500 The research results provide a theoretical basis for structural optimization and system matching of catalytic
 501 converters.



502
 503 **Fig. 16** Influence correlation degree

504 **5. Conclusion**

505 By establishing a new catalytic converter model, the uniformity of internal flow field is improved, to
 506 achieve the purpose of improving NO catalysis. In addition, the optimum structural parameters are
 507 determined by quantitative analysis of NO conversion rate and NO₂ mass fraction at the outlet of the carrier,
 508 to further optimize the model. The specific results are as follows:

509 (1) Compared with the standard catalytic converter, the gas uniformity, NO conversion rate and carrier
 510 pressure drop of the improved catalytic converter increased by 0.0643, 7.0% and 6.78%, respectively. It
 511 improves NO catalytic and reduces vehicle emission.

512 (2) When the high and low cell densities are different, the performance is better when the cell density
 513 combination is larger. When the low cell density is the same, the smaller the high cell density, the better the
 514 performance. When the cell density combination is 700 cps/600 cps, its performance is better; the gas

515 uniformity and NO conversion rate reach the highest, which are 0.9821 and 73.7%, and the carrier pressure
516 drop is 232 Pa.

517 (3) When the tapered height increases from 5 mm to 25 mm, the catalytic converter performance increases
518 first and then decreases under the exhaust inlet velocity of $10.28 \text{ m}\cdot\text{s}^{-1}$. Its performance is better when the
519 tapered height is 20 mm; the NO conversion rate reaches the highest, 72.4%, the gas uniformity and carrier
520 pressure drop are 0.9774 and 212 Pa, respectively.

521 (4) With the increase of high cell density radius, the performance of catalytic converter increases first and
522 then decreases under the exhaust inlet velocity of $10.28 \text{ m}\cdot\text{s}^{-1}$. Its performance is better when the radius of
523 high cell density radius is 20 mm; the NO conversion rate reaches the highest, 72.1%, the gas uniformity
524 and carrier pressure drop are 0.9783 and 198 Pa, respectively.

525 (5) With the increase of tapered end face radius, the performance of improved catalytic converter increases
526 first and then decreases under the exhaust inlet velocity of $10.28 \text{ m}\cdot\text{s}^{-1}$. Its performance is better when the
527 radius of tapered end face radius is 20 mm; the NO conversion rate reaches the highest, 72.0%, the gas
528 uniformity and carrier pressure drop are 0.9784 and 189 Pa, respectively.

529 (6) Grey correlation analysis results show that low cell density is the key factor affecting the improved
530 catalytic converter.

531 **Authors' contributions**

532 **Qingsong Zuo**: Resources, Funding acquisition, Project administration, Data curation, Writing-Original
533 Draft, Writing-Review & Editing. **Xiaomei Yang**: Software, Data curation, Writing-Original Draft,
534 Writing-Review & Editing. **Bin Zhang**: Resources, Funding acquisition, Project administration. **Qingwu**
535 **Guan**: Conceptualization, Methodology. **Zhuang Shen**: Formal analysis, Software. **Yongchuan Xie**:
536 Software. **Qiming Li**: Data curation.

537 **Consent to Participate and Consent to Publish**

538 Not applicable

539 **Availability of data and materials**

540 All data generated or analyzed during this study are included in this published article.

541 **Competing interests**

542 The authors declare that they have no competing interests.

543 **Ethical Approval**

544 Not applicable

545 **Funding**

546 This work is supported by the National Natural Science Foundation of China (Grant No. 52076184), the
547 Natural Science Foundation of Hunan Province (Grant No. 2020JJ6002), the Hunan Provincial Key
548 Laboratory of Vehicle Power and Transmission System (Grant No. VPTS202004).

549 **Reference**

550 Almeida PR, Nakamura AL, Sodre JR. (2014) Evaluation of catalytic converter aging for vehicle operation
551 with ethanol. *Appl Therm Eng* 71:335-341. <https://doi.org/10.1016/j.applthermaleng.2014.06.069>

552 Andrew R, Richard B, Philip S. (2014) Internal combustion engine cold-start efficiency: A review of the
553 problem, causes and potential solutions. *Energy Convers Manage* 82:327-350.
554 <https://doi.org/10.1016/j.enconman.2014.03.002>

555 Ayodhya AS, Narayanappa KG. (2018) An overview of after-treatment systems for diesel engines. *Environ*
556 *Sci Pollut Res* 25(35):35034–35047. <https://doi.org/10.1007/s11356-018-3487-8>

557 Baumard P, Budzinski H, Garrigues P. (1998) Polycyclic aromatic hydrocarbons (PAHs) in sediments and
558 mussels of the western Mediterranean Sea. *Environ Toxicol Chem* 17:765-776.
559 <https://doi.org/10.1002/etc.5620170501>

560 Bogarra M, Herreros J M, Hergueta C. (2017) Influence of Three-Way Catalyst on Gaseous and Particulate

561 Matter Emissions During Gasoline Direct Injection Engine Cold-start. Johnson Matthey Tech
562 61(4):329-341. <https://doi.org/10.1595/205651317X696315>

563 Cai T, Zhao D, E JQ. (2020) Bluff-body effect on thermal and NO_x emission characteristics in a micro-
564 planar combustor fueled with premixed ammonia-oxygen. Chem Eng Process 153.
565 <https://doi.org/10.1016/j.cep.2020.107979>.

566 Deng YW, Zheng WP, E JQ, Zhang B, Zhao XH, Zuo QS, Zhang ZQ, Han DD. (2017) Influence of
567 geometric characteristics of a diesel particulate filter on its behavior in equilibrium state. Appl Therm
568 Eng 123:61-73. <https://doi.org/10.1016/j.applthermaleng.2017.05.071>

569 Dey S, Chandra Dhal G. (2020) Controlling carbon monoxide emissions from automobile vehicle exhaust
570 using copper oxide catalysts in a catalytic converter. Mater Today Chem 17:
571 <https://doi.org/10.1016/j.mtchem.2020.100282>.

572 E JQ, Zheng PY, Han DD, Zhao XH, Deng YW. (2020) Effect analysis on soot combustion performance
573 enhancement in a rotary diesel particulate filter unit during continuous microwave heating. Fuel.
574 <https://doi.org/10.1016/j.fuel.2020.118043>.

575 Gao JB, Tian GH, Sorniotti A, Karci AE, Palo RD. (2019) Review of thermal management of catalytic
576 converters to decrease engine emissions during cold start and warm up. Appl Therm Eng 147:177-
577 187. <https://doi.org/10.1016/j.applthermaleng.2018.10.037>

578 Hesham A, Ibrahim, Wael HA, Sherif A. (2018) Experimental and numerical investigations of flow through
579 catalytic converters. Int J Heat Mass Tran 127:546-560.
580 <https://doi.org/10.1016/j.ijheatmasstransfer.2018.07.052>

581 Kadier A, Abdeshahian P, Simayi Y, Ismail M, Hamid AA, Kalil MS. (2015) Grey relational analysis for
582 comparative assessment of different cathode materials in microbial electrolysis cells. Energy
583 90(2):1556-1562. <https://doi.org/10.1016/j.energy.2015.06.108>

- 584 Kumar C, Rana KB, Tripathi B. (2019) Effect of diesel-methanol-nitromethane blends combustion on VCR
585 stationary CI engine performance and exhaust emissions. *Environ Sci Pollut Res* 26:6517–6531.
586 <https://doi.org/10.1007/s11356-018-04058-1>
- 587 Liang YL, Ding XM, Dai JY, Zhao M, Zhong L, Wang JL, Chen YQ. (2019) Active oxygen-promoted NO
588 catalytic on monolithic Pt-based diesel oxidation catalyst modified with Ce. *Catal Today* 327:64-72.
589 <https://doi.org/10.1016/j.cattod.2018.06.008>
- 590 Lichtfouse E, Budzinski H, Garrigues P, Eglinton T. (1997) Ancient polycyclic aromatic hydrocarbons in
591 modern soils: ¹³C, ¹⁴C and biomarker evidence. *Organic Geochemistry* 26:353-359.
592 [https://doi.org/10.1016/S0146-6380\(97\)00009-0](https://doi.org/10.1016/S0146-6380(97)00009-0)
- 593 Liu HY, Li ZY, Xu HM, Ma X, Shuai SJ. (2020) Nucleation mode particle evolution in a gasoline direct
594 injection engine with/without a three-way catalyst converter. *Appl Energy* 259.
595 <https://doi.org/10.1016/j.apenergy.2019.114211>.
- 596 Liu HY, Li ZY, Zhang MZ, Xu HM, Ma X, Shuai SJ. (2021) Exhaust non-volatile particle filtration
597 characteristics of three-way catalyst and influencing factors in a gasoline direct injection engine
598 compared to gasoline particulate filter. *Fuel* 290. <https://doi.org/10.1016/j.fuel.2020.120065>.
- 599 Manojkumar R, Haranethra S, Muralidharan M, Ramaprabhu A. I.C. (2020) Engine emission reduction
600 using catalytic converter by replacing the noble catalyst and using copper oxide as the catalyst. *Mater*
601 *Today: Proceedings*. <https://doi.org/10.1016/j.matpr.2020.02.804>.
- 602 Matsuzawa S, Nasser-Ali L, Garrigues P. (2001) Photolytic behavior of polycyclic aromatic hydrocarbons
603 in diesel particulate matter deposited on the ground. *Environ Sci Technol* 35(15):3139-3143.
604 <https://doi.org/10.1021/es001606q>
- 605 Matthew SR, Kara MK. (2016) The problem of cold starts: A closer look at mobile source emissions levels.
606 *Transport Res D-Tr E* 43:123-132. <https://doi.org/10.1016/j.trd.2015.12.012>

607 Miles WM, William DJ. (2017) Catalytic oxidation of carbon monoxide by α -alumina supported 3nm
608 cerium dioxide nanoparticles. *Mol Catal* 493:9-14. <https://doi.org/10.1016/j.mcat.2017.06.015>

609 Mu M, Li X, Qiu Y, Shi Y. (2019a) Study on a new gasoline particulate filter structure based on the nested
610 cylinder and diversion channel plug. *Energies* 12(11):1-19. <https://doi.org/10.3390/en12112045>

611 Mu M, Sjöblom J, Ström H, Li X. (2019b) Analysis of the flow field from Connection Cones to Monolith
612 Reactors. *Energies* 12(3):1-20. <https://doi.org/10.3390/en12030455>

613 Park H, Bae C, Ha C. (2019) A comprehensive analysis of multiple injection strategies for improving diesel
614 combustion process under cold-start conditions. *Fuel*. <https://doi.org/10.1016/j.fuel.2019.115762>.

615 Qian Y, Li ZL, Yu L, Wang XL, Lu XC. (2019a) Review of the state-of-the-art of particulate matter
616 emissions from modern gasoline fueled engines. *Appl Energy* 238:1269-1298.
617 <https://doi.org/10.1016/j.apenergy.2019.01.179>

618 Qian Y, Wu ZY, Guo JJ, Li ZL, Jiang CX, Lu XC. (2019b) Experimental studies on the key parameters
619 controlling the combustion and emission in premixed charge compression ignition concept based on
620 diesel surrogates. *Appl Energy* 235:233-246. <https://doi.org/10.1016/j.apenergy.2018.10.104>

621 Santos H, Costa M. (2008) Evaluation of the conversion efficiency of ceramic and metallic three ways
622 catalytic converters. *Energ Convers Manage* 49(2):291-300.
623 <https://doi.org/10.1016/j.enconman.2007.06.008>

624 Shen ZG, Tian LL, Liu X. (2019) Automotive exhaust thermoelectric generators: Current status, challenges
625 and future prospects. *Energ Convers Manage* 195:1138-1173.
626 <https://doi.org/10.1016/j.enconman.2019.05.087>

627 Su QY, Xie L, Shuai SJ, Wang JX, Song JO, Li ZJ. (2013) Optimization of automotive catalytic converter
628 by numerical modeling and simulation with detailed mechanism. *Catal Today* 216:292-298.
629 <https://doi.org/10.1016/j.cattod.2013.06.015>

630 Subhashish D, Ganesh CD, Devendra M, Ram P. (2019) Application of hopcalite catalyst for controlling
631 carbon monoxide emission at cold-start emission conditions. *J. Traffic Transp Eng* 6(5):419-440.
632 <https://doi.org/10.1016/j.jtte.2019.06.002>

633 Sun YZ, Zhao D, Zhu XW. (2021) Generation and Mitigation Mechanism Studies of Nonlinear
634 Thermoacoustic Instability in a Modelled Swirling Combustor with a Heat Exchanger. *Aerospace* 8.
635 <https://doi.org/10.3390/aerospace8030060>.

636 Takeru Y, Hiromasa S, Yuki A, Naohiro H. (2017) Development of a New Ceramic Substrate with Gas
637 Flow Control Functionality. *SAE Int J Engines* 10:1588-1594. <https://doi.org/10.4271/2017-01-0919>

638 Tang AK, Cai T, Deng J, Zhao D, Huang QH, Zhou C. (2019) Experimental study of flame structure
639 transitions of premixed propane/air in micro-scale planar combustors. *Energy* 179:558-570.
640 <https://doi.org/10.1016/j.energy.2019.05.005>

641 Wang ZQ, Hu YH, Xia XX, Zuo QS, Zhao B, Li ZX. (2020) Thermo-economic selection criteria of
642 working fluid used in dual-loop ORC for engine waste heat recovery by multi-objective optimization.
643 *Energy* 197. <https://doi.org/10.1016/j.energy.2020.117053>.

644 Xu JM, Yuan ZQ, Dai TQ. (2009) Numerical simulation of catalytic converters with different carrier end
645 shapes. *Journal of Shanxi University of science and Technology* 27 (06): 87-90.
646 <https://doi.org/10.3969/j.issn.1000-5811.2009.06.021>

647 Zhang B, E JQ, Gong JK, Yuan WH, Zhao XH, Hu WY. (2017) Influence of structural and operating
648 factors on performance degradation of the diesel particulate filter based on composite regeneration.
649 *Appl Therm Eng* 121:838-852. <https://doi.org/10.1016/j.applthermaleng.2017.04.155>

650 Zhang ZQ, Ye JD, Tan DL, Feng ZQ, Luo JB, Tan Y, Huang YX. (2021) The effects of Fe₂O₃ based DOC
651 and SCR catalyst on the combustion and emission characteristics of a diesel engine fueled with
652 biodiesel. *Fuel*. <https://doi.org/10.1016/j.fuel.2020.120039>.

653 Zhao D, Guan Y, Reinecke A. (2019) Characterizing hydrogen-fuelled pulsating combustion on
654 thermodynamic properties of a combustor. *Commun Phys* 2 44.
655 <https://doi.org/10.1038/s42005.019.0142.8>.

656 Zhong C, Gong J, Wang S. et al. (2021) NO₂ catalytic formation, consumption, and efflux in various types
657 of diesel particulate filter. *Environ Sci Pollut Res*. <https://doi.org/10.1007/s11356-020-11870-1>.

658 Zhong WJ, Tamilselvan P, Wang Q, He ZX, Feng H, Yu X. (2018) Experimental study of spray
659 characteristics of diesel/hydrogenated catalytic biodiesel blended fuels under inert and reacting
660 conditions. *Energy* 153:349-358. <https://doi.org/10.1016/j.energy.2018.04.045>

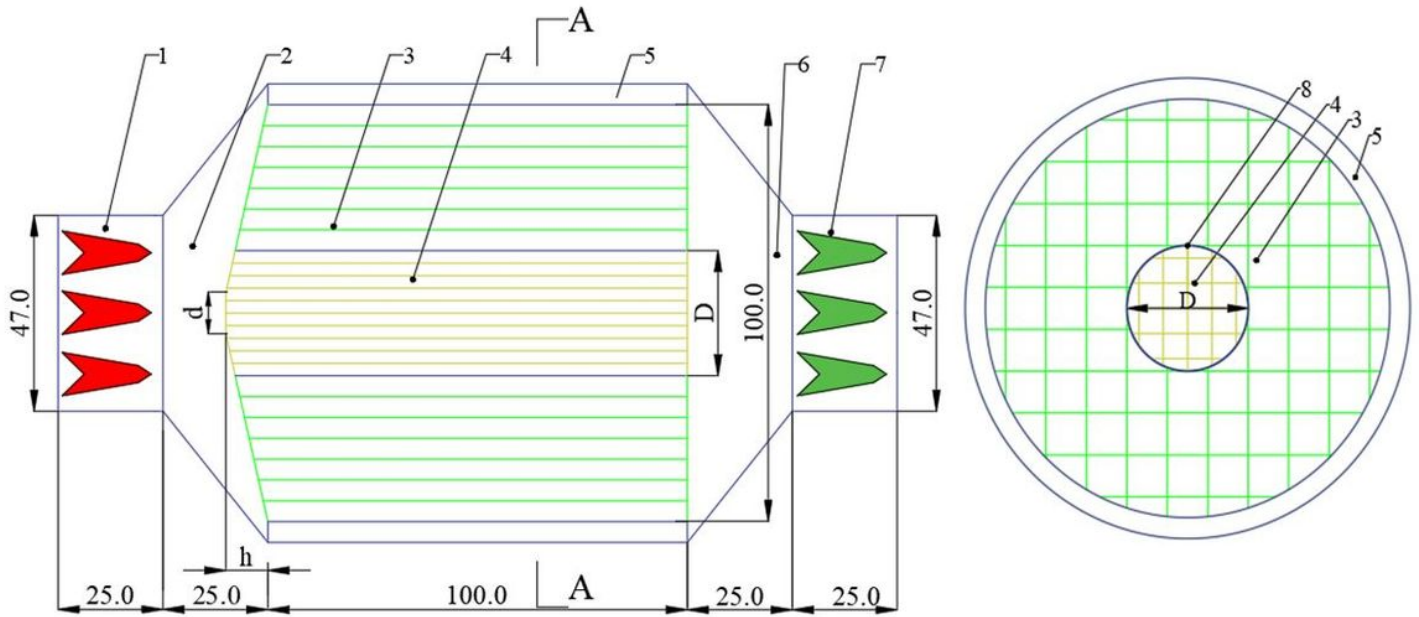
661 Zhong WJ, Xuan TM, He ZX, Wang Q, Li D, Zhang X, Huang YY. (2016) Experimental study of
662 combustion and emission characteristics of diesel engine with diesel/second-generation biodiesel
663 blending fuels. *Energ Convers Manage* 121:241-250.
664 <https://doi.org/10.1016/j.enconman.2016.05.033>

665 Zuo QS, Xie Y, E JQ, Zhu XN, Zhang B, Tang YY, Zhu CH, Wang ZQ, Zhang JP. (2019a) Effect of
666 different exhaust parameters on NO conversion efficiency enhancement of a dual-carrier catalytic
667 converter in the gasoline engine. *Energy*. <https://doi.org/10.1016/j.energy.2019.116521>.

668 Zuo QS, Xie Y, Guan QX, Zhu GH, Ye JQ, Zhu XN, Tang YY, Wang ZQ, Chen W. (2019b) Effect of
669 critical dual-carrier structure parameters on performance enhancement of a dual-carrier catalytic
670 converter and the gasoline engine system. *Energ Convers Manage*.
671 <https://doi.org/10.1016/j.enconman.2019.112325>.

672 Zuo W, E JQ, Liu XL, Peng QG, Deng YW, Zhu H. (2016) Orthogonal Experimental Design and Fuzzy
673 Grey Relational Analysis for emitter efficiency of the micro-cylindrical combustor with a step. *Appl*
674 *Therm Eng* 103:945-951. <https://doi.org/10.1016/j.applthermaleng.2016.04.148>

Figures



1-inlet pipe, 2-expansion pipe, 3-low cell density carrier, 4-high cell density carrier,

5-liner, 6-contraction pipe, 7-outlet pipe, 8-interface of high and low cell density

Figure 1

Structure of tapered variable cell density carrier catalytic converter

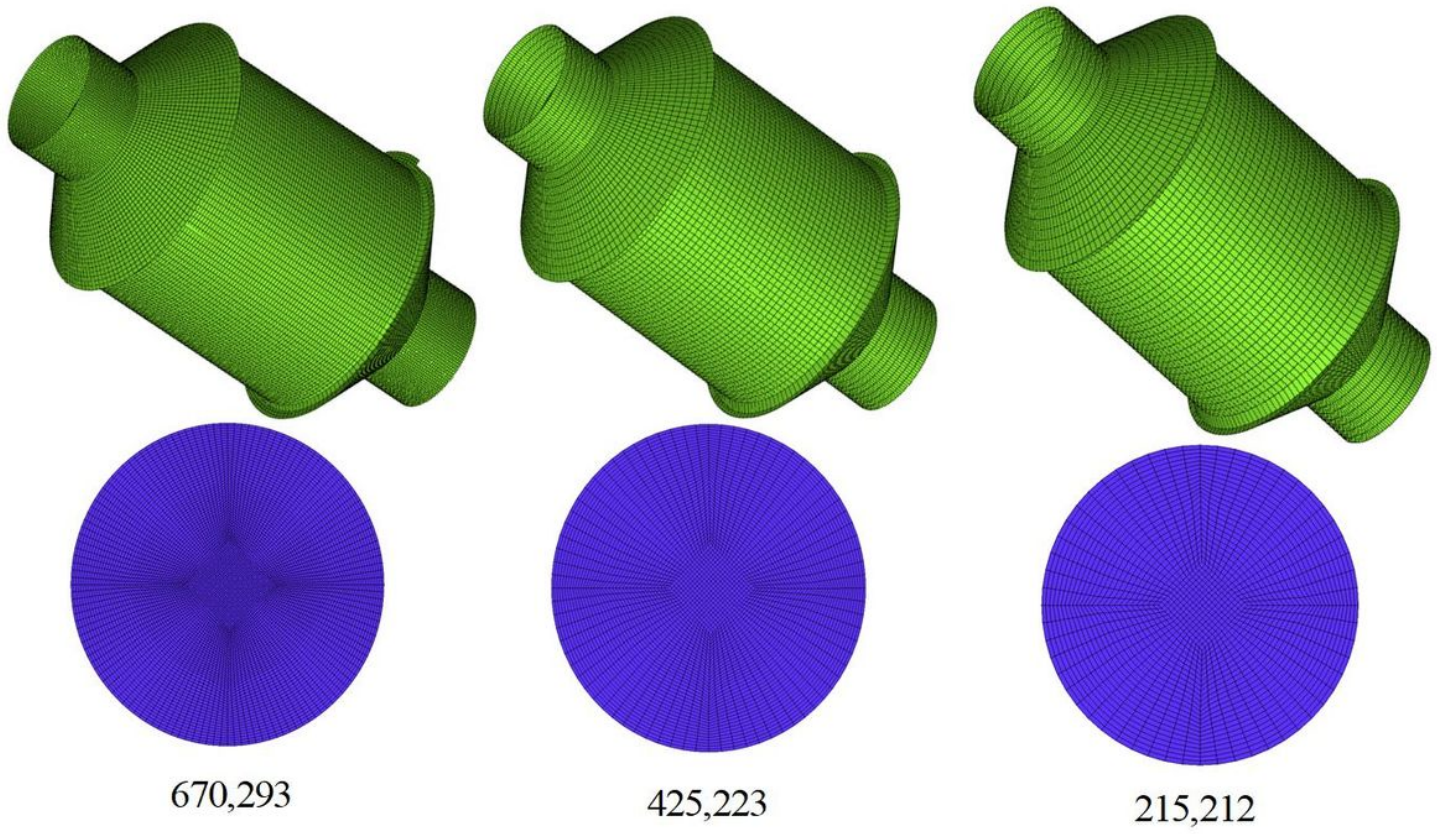
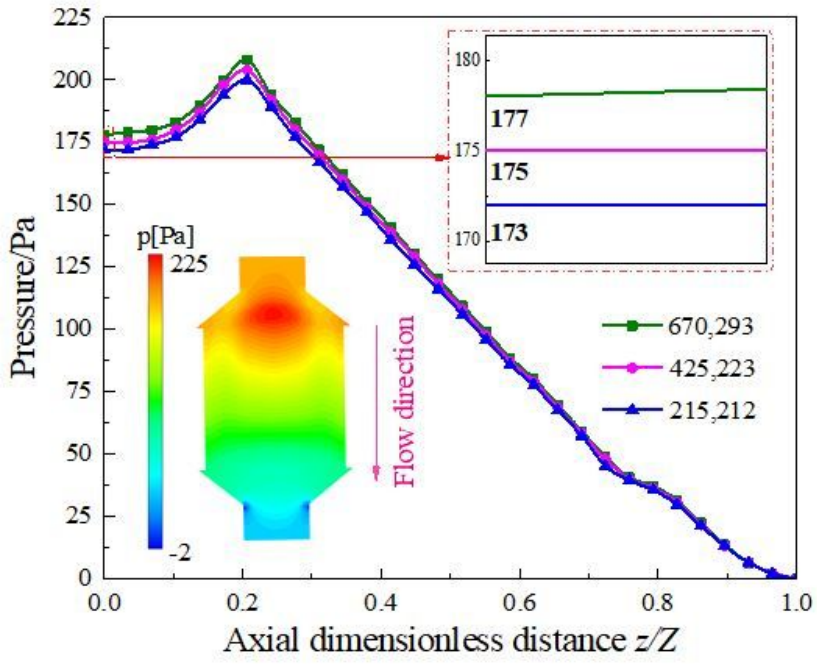
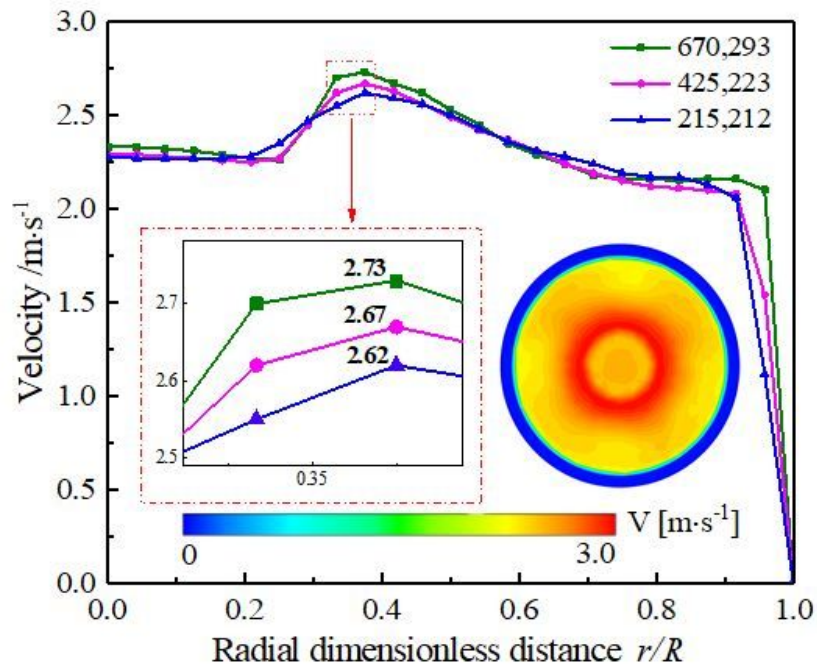


Figure 2

Three different mesh models



(a) Axial distribution of pressure



(b) Radial distribution of velocity

Figure 3

Grid independence verification

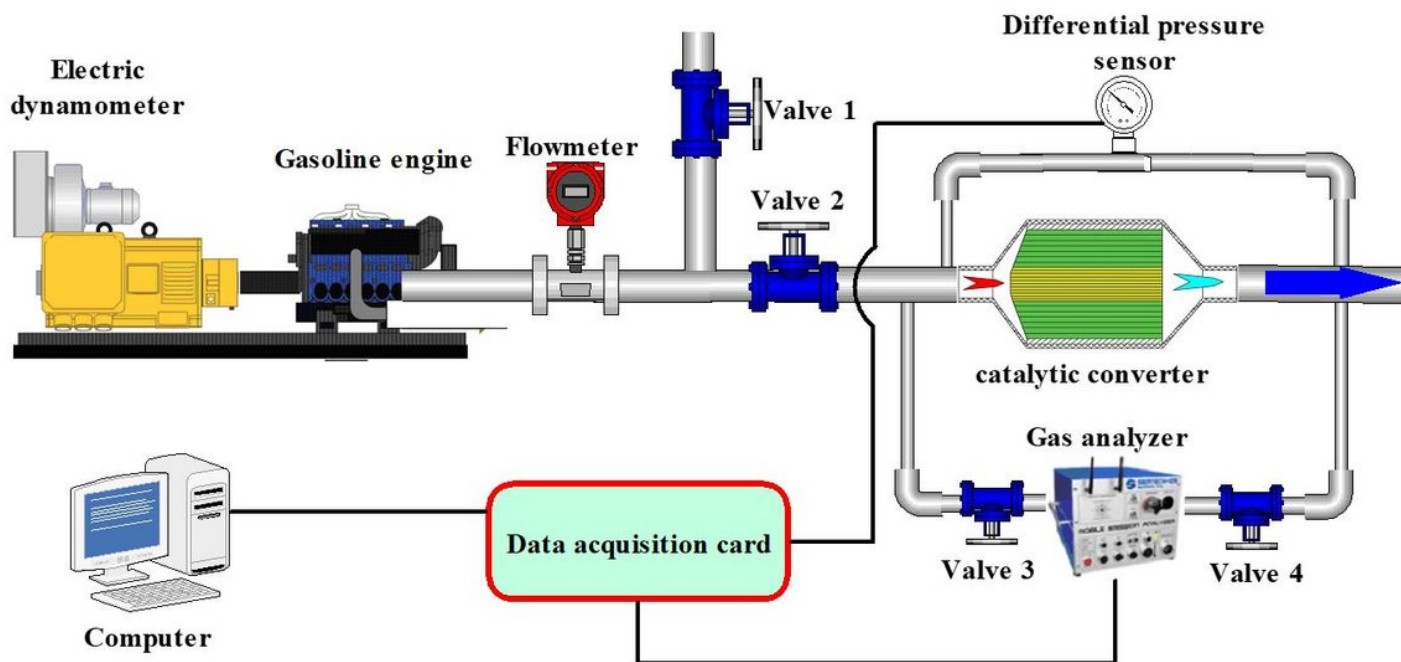
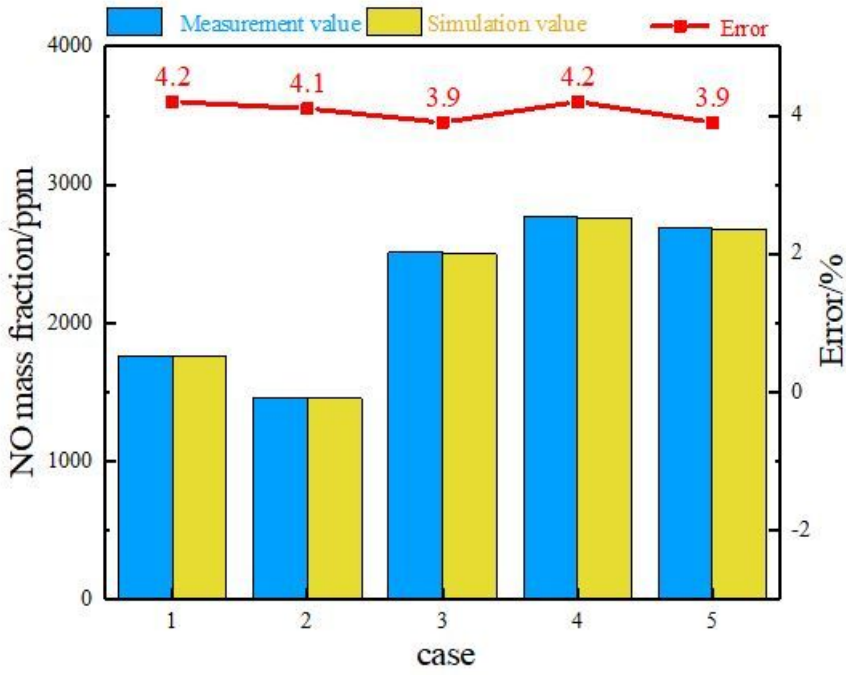
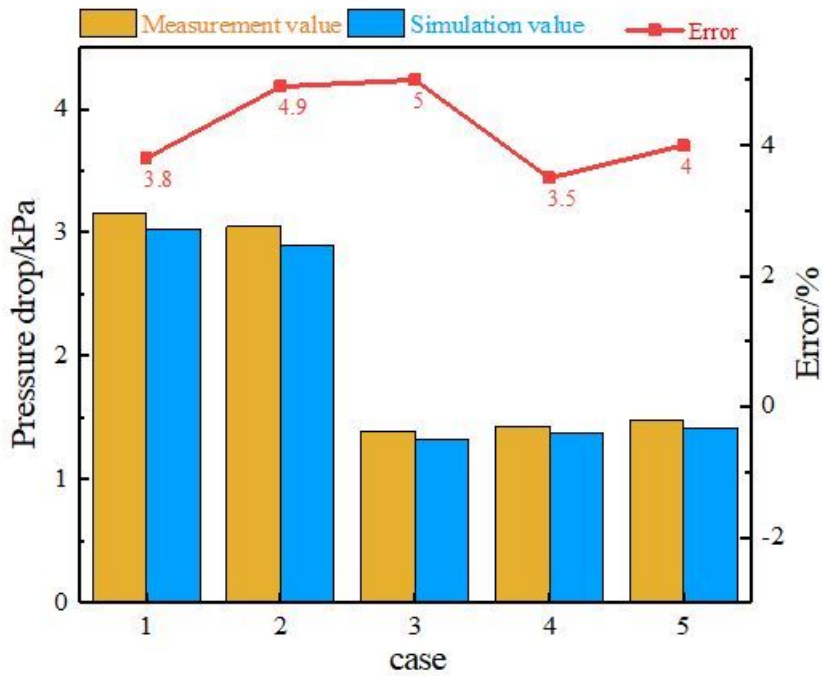


Figure 4

Schematic of the experimental apparatus



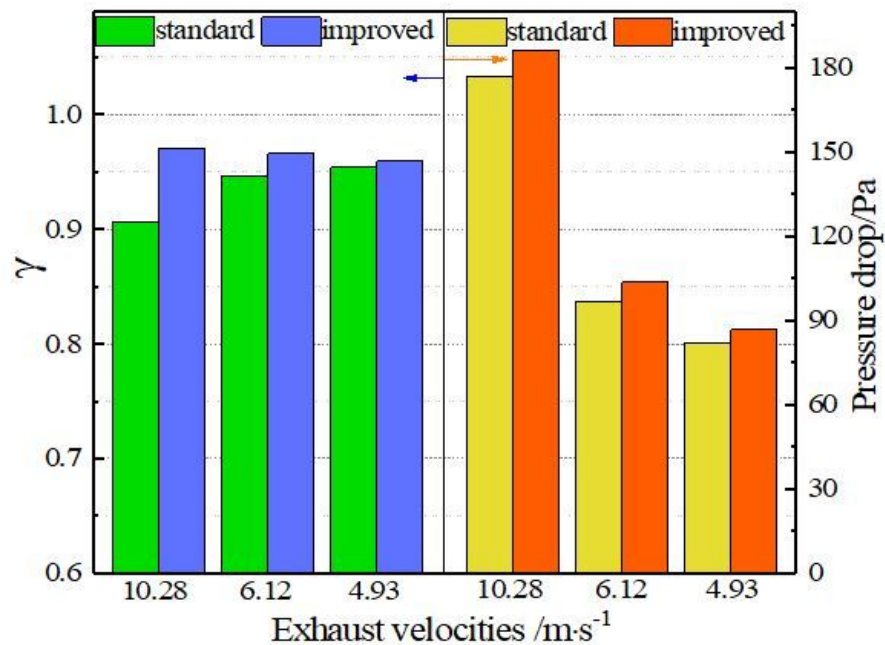
(a) NO mass fraction and error



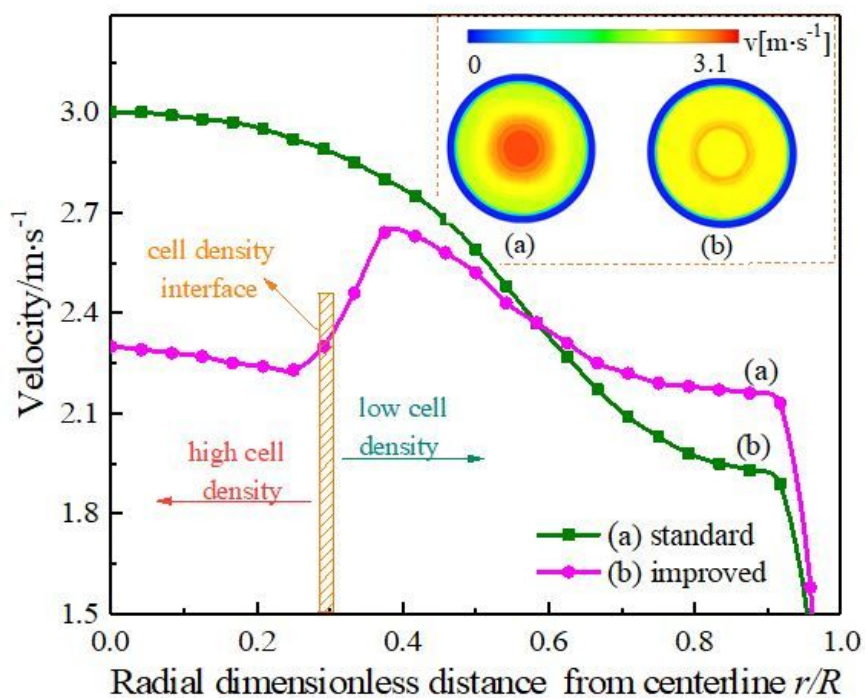
(b) Pressure drop and error

Figure 5

Catalytic converter outlet NO mass fraction and pressure drop



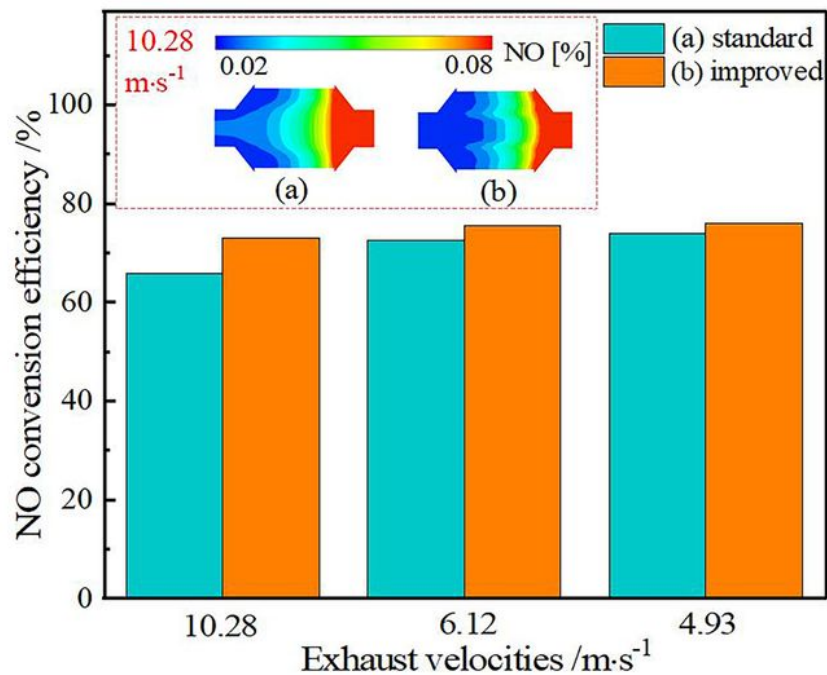
(a) Carrier pressure drop and gas uniformity under three cases



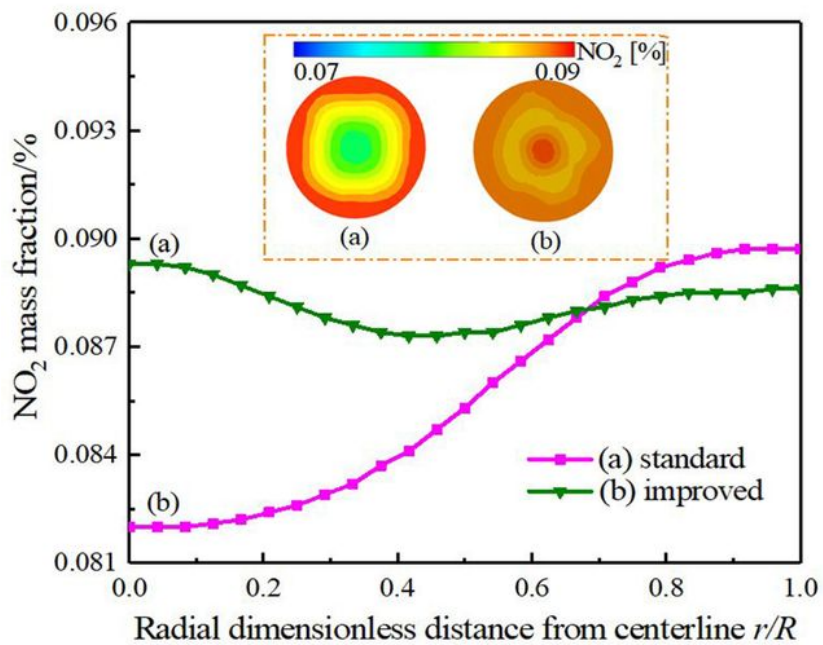
(b) Radial distribution of velocities at the carrier outlet

Figure 6

Comparison of gas uniformity and carrier pressure drop



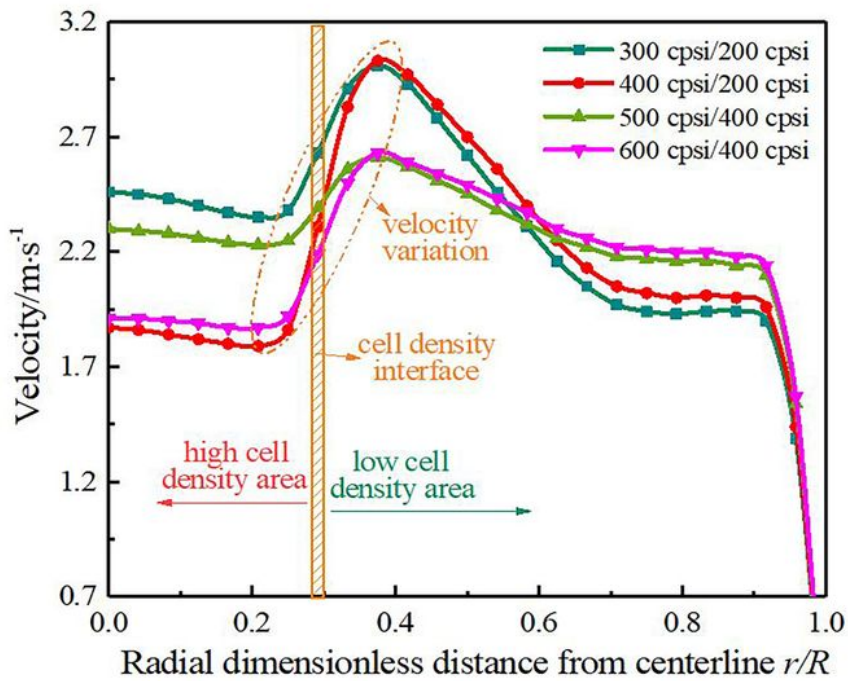
(a) NO conversion rates under three cases



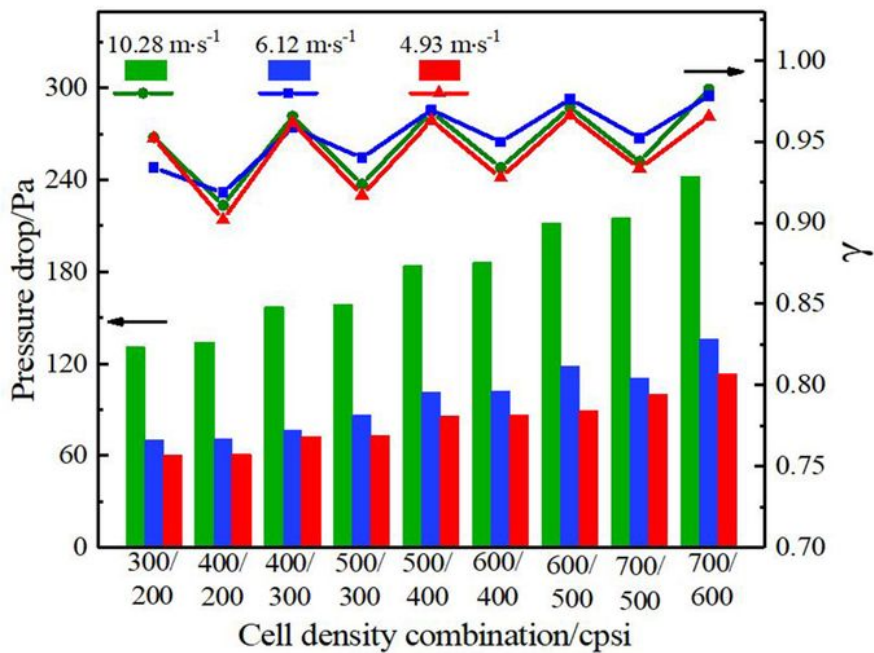
(b) Radial distribution of NO₂ mass fraction at exit

Figure 7

Comparison of NO conversion rate and NO₂ mass fraction



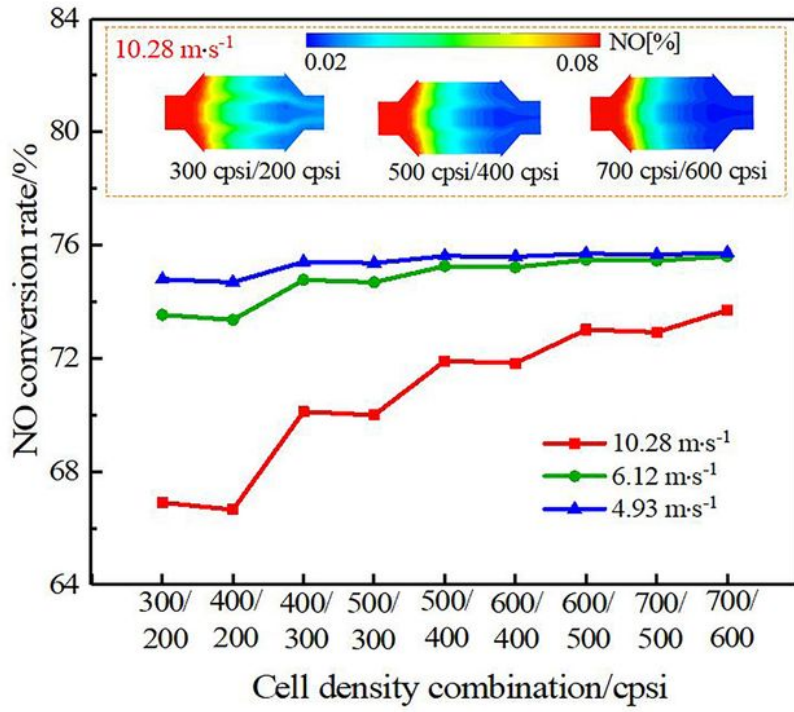
(a) Radial distribution of carrier outlet velocity



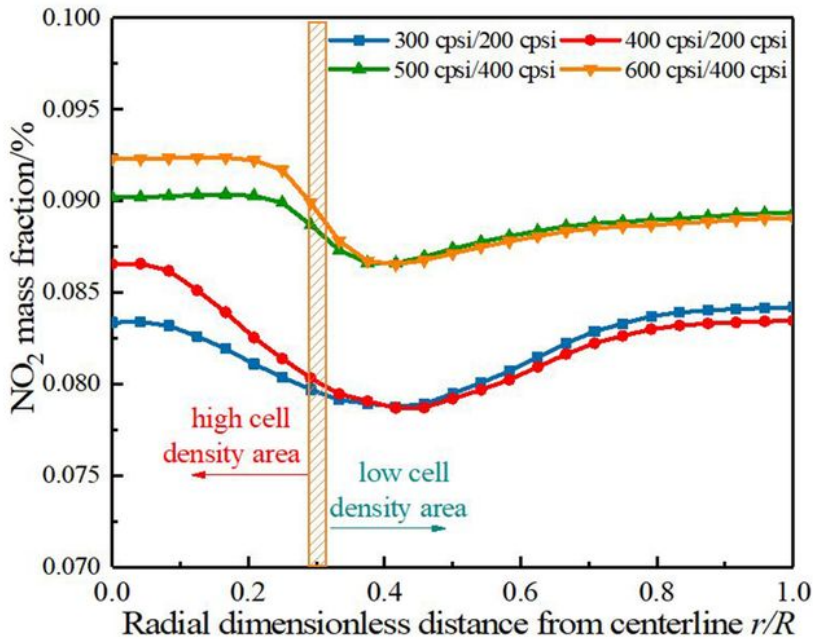
(b) Carrier pressure drop and gas uniformity

Figure 8

Gas uniformity and carrier pressure drop



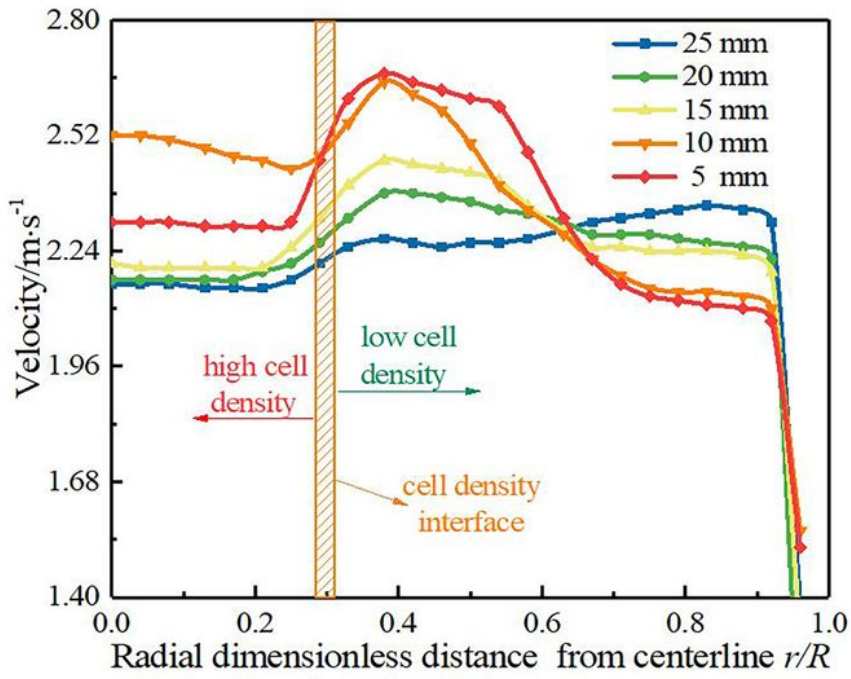
(a) NO conversion rate



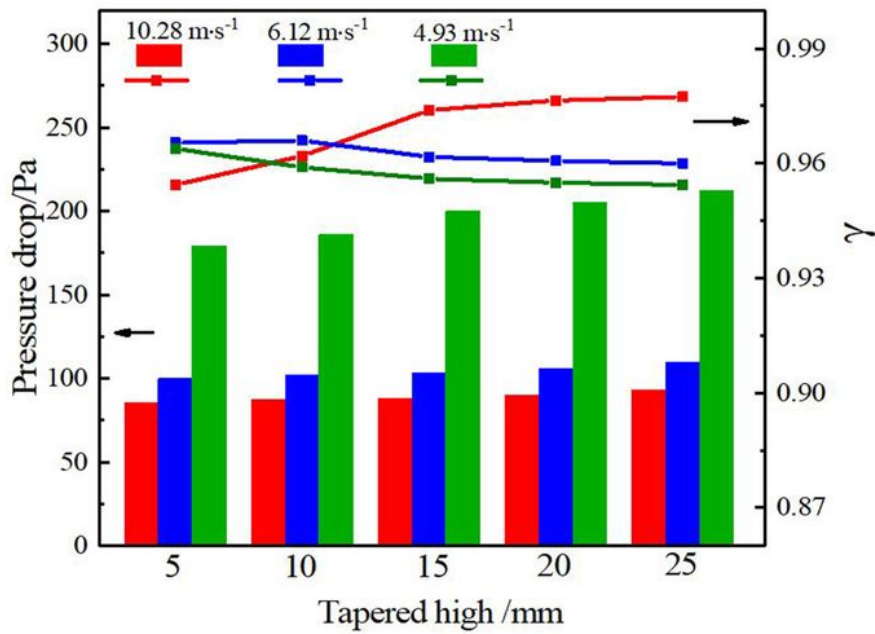
(b) Distribution of NO₂ mass fraction at export

Figure 9

NO conversion rate and NO₂ mass fraction



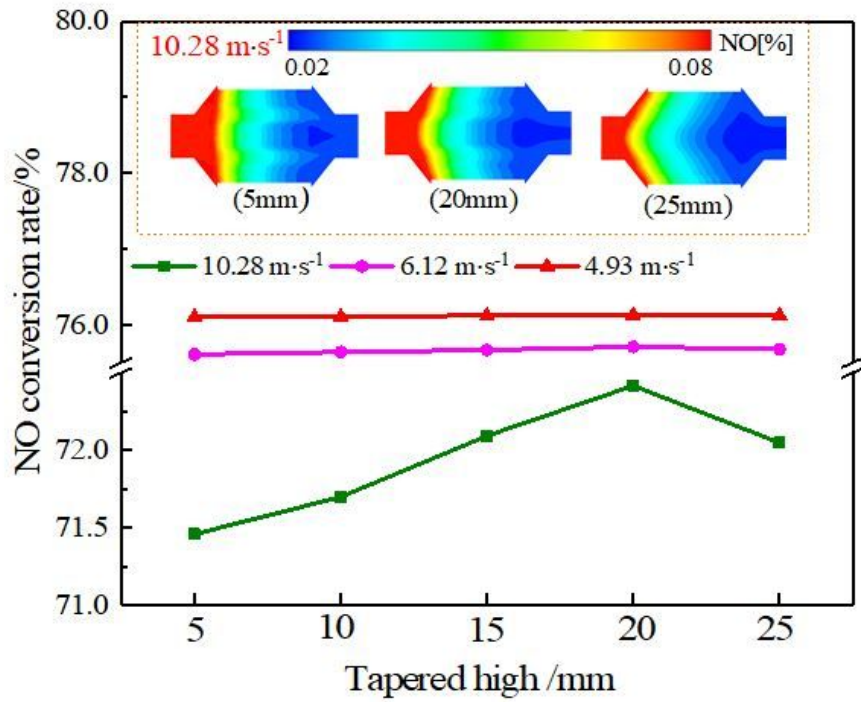
(a) Radial distribution of velocity at carrier exit



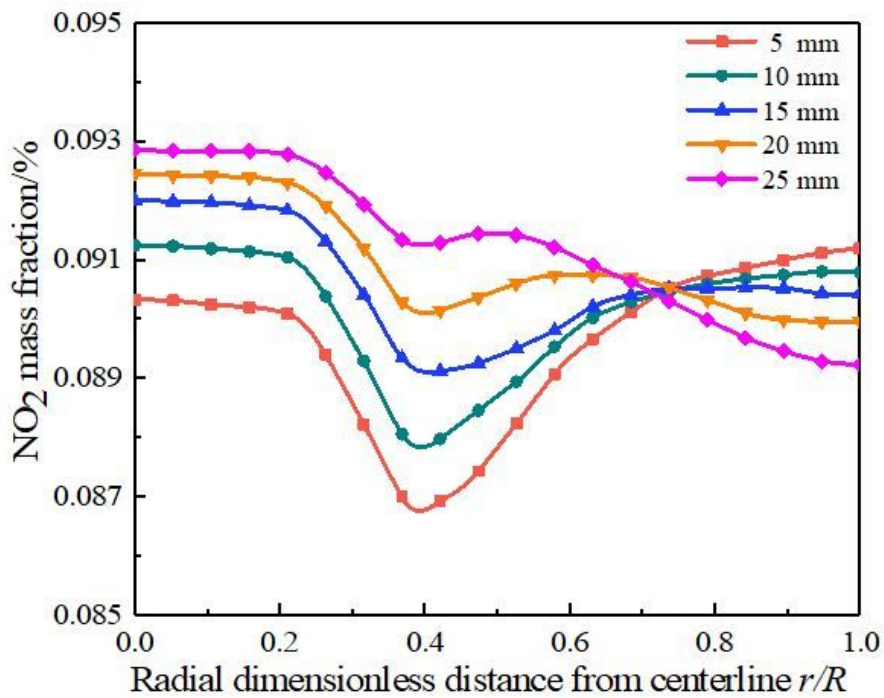
(b) Gas uniformity and carrier pressure drop

Figure 10

Gas uniformity and carrier pressure drop



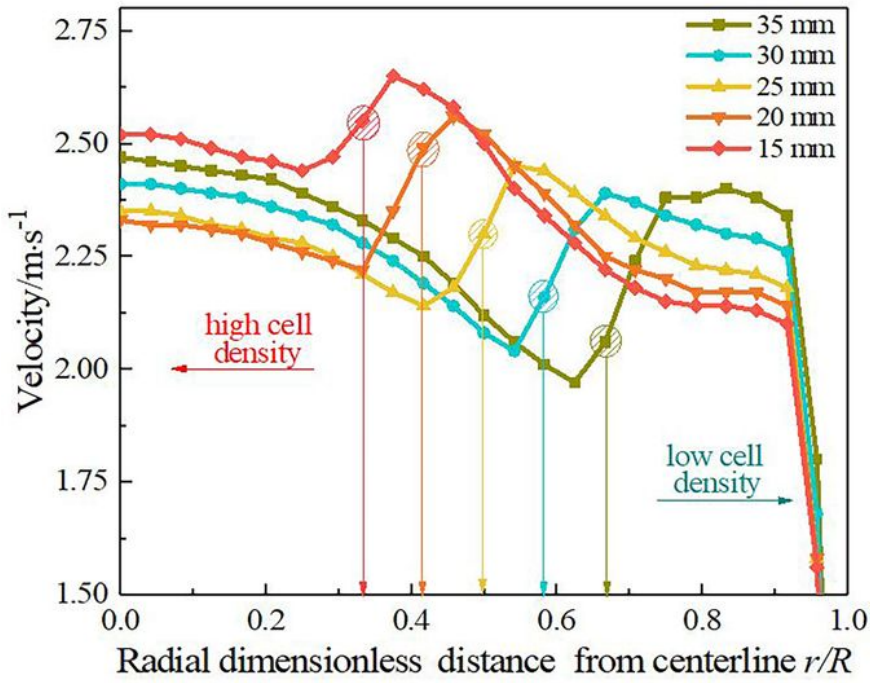
(a) NO conversion rate



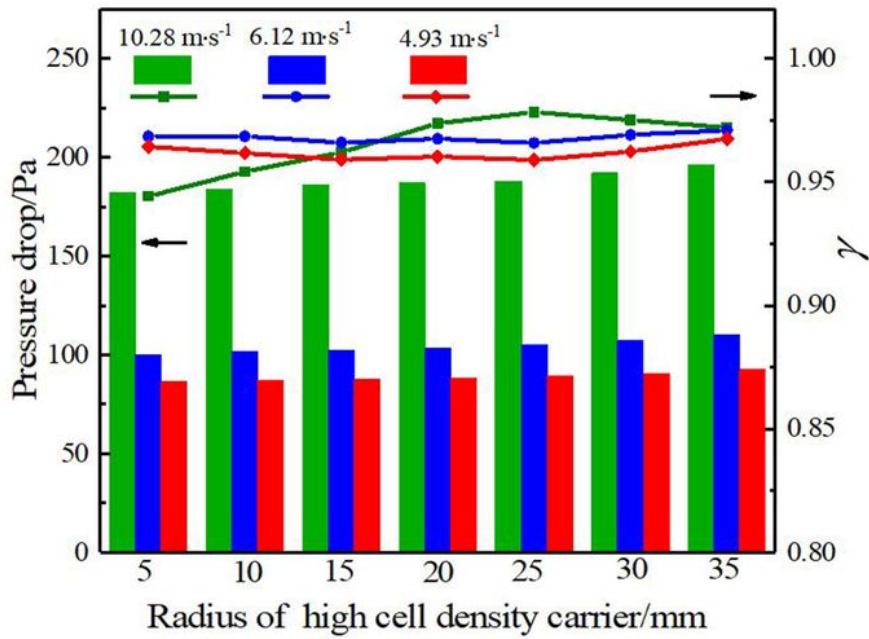
(b) Radial distribution of NO₂ mass fraction at carrier outlet

Figure 11

NO conversion rate and NO₂ mass fraction



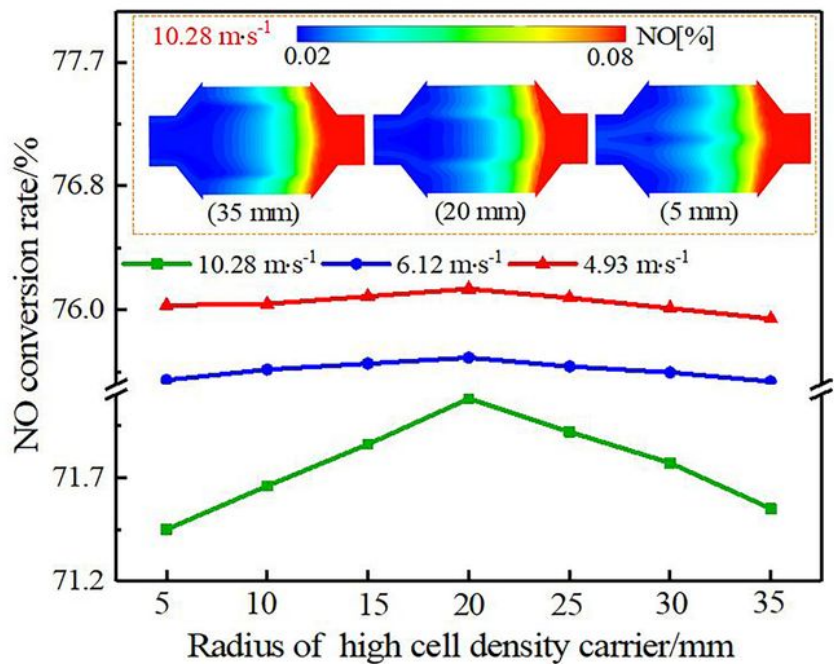
(a) Radial distribution of velocity at carrier exit



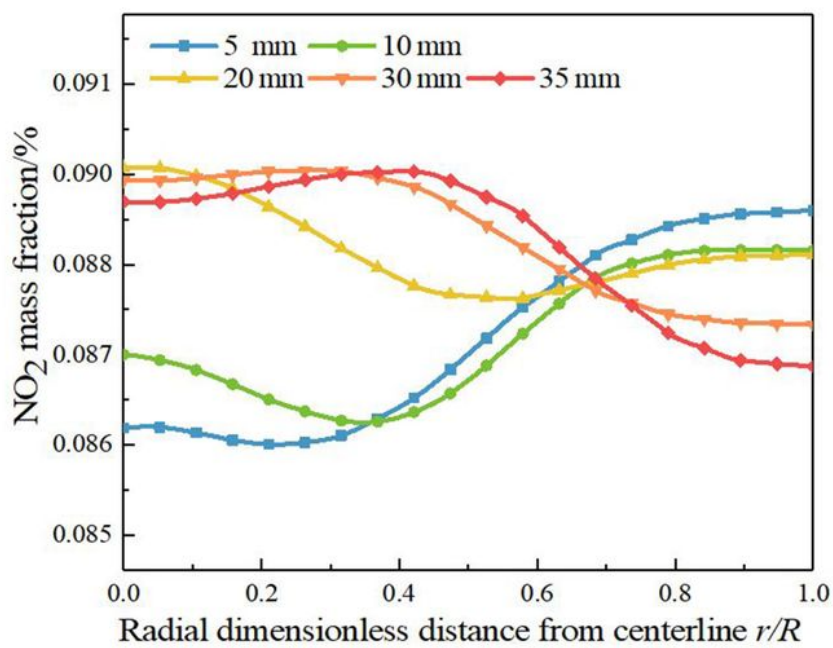
(b) Gas uniformity and carrier pressure drop

Figure 12

Gas uniformity and carrier pressure drop



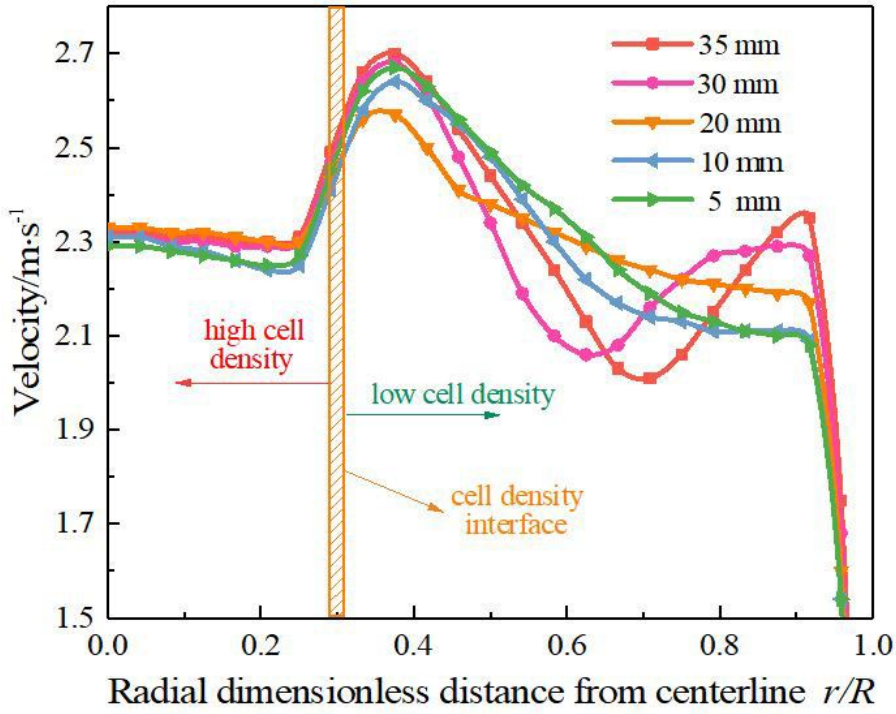
(a) NO conversion rate



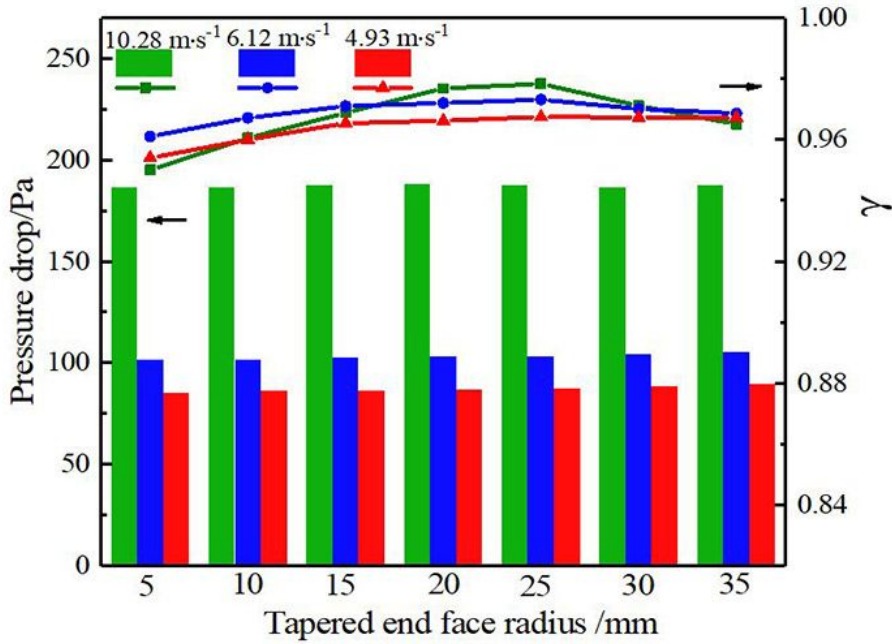
(b) Radial distribution of NO₂ mass fraction at the outlet

Figure 13

NO conversion rate and NO₂ mass fraction



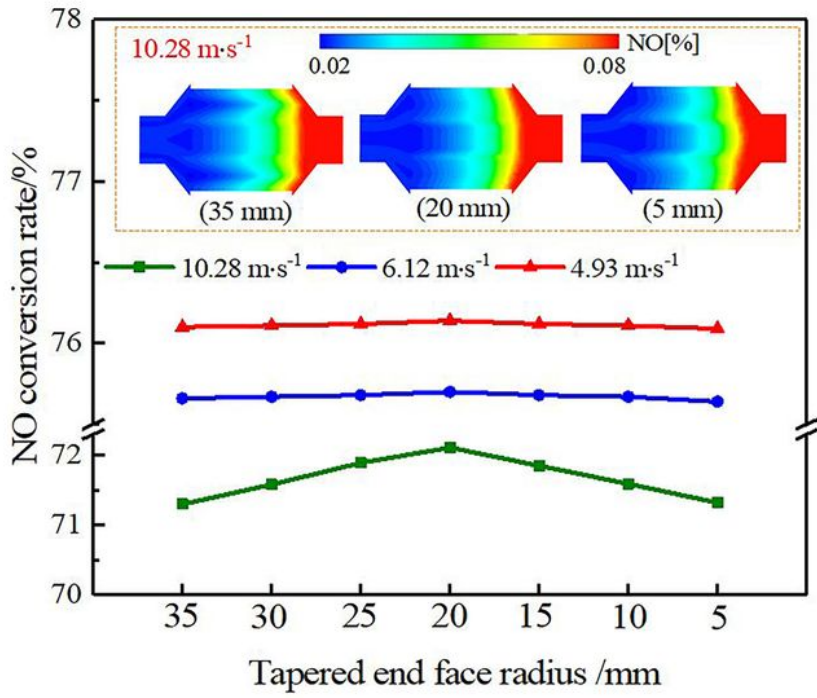
(a) Radial distribution of velocity at carrier exit



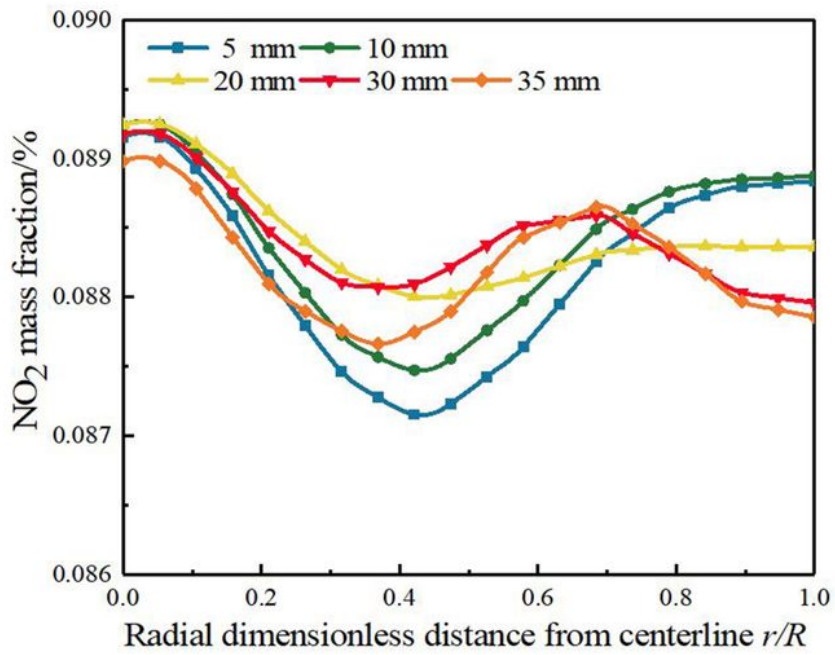
(b) Gas uniformity and carrier pressure drop

Figure 14

Gas uniformity and carrier pressure drop



(a) NO conversion rate



(b) Radial distribution of NO₂ mass fraction at outlet

Figure 15

NO conversion rate and NO₂ mass fraction

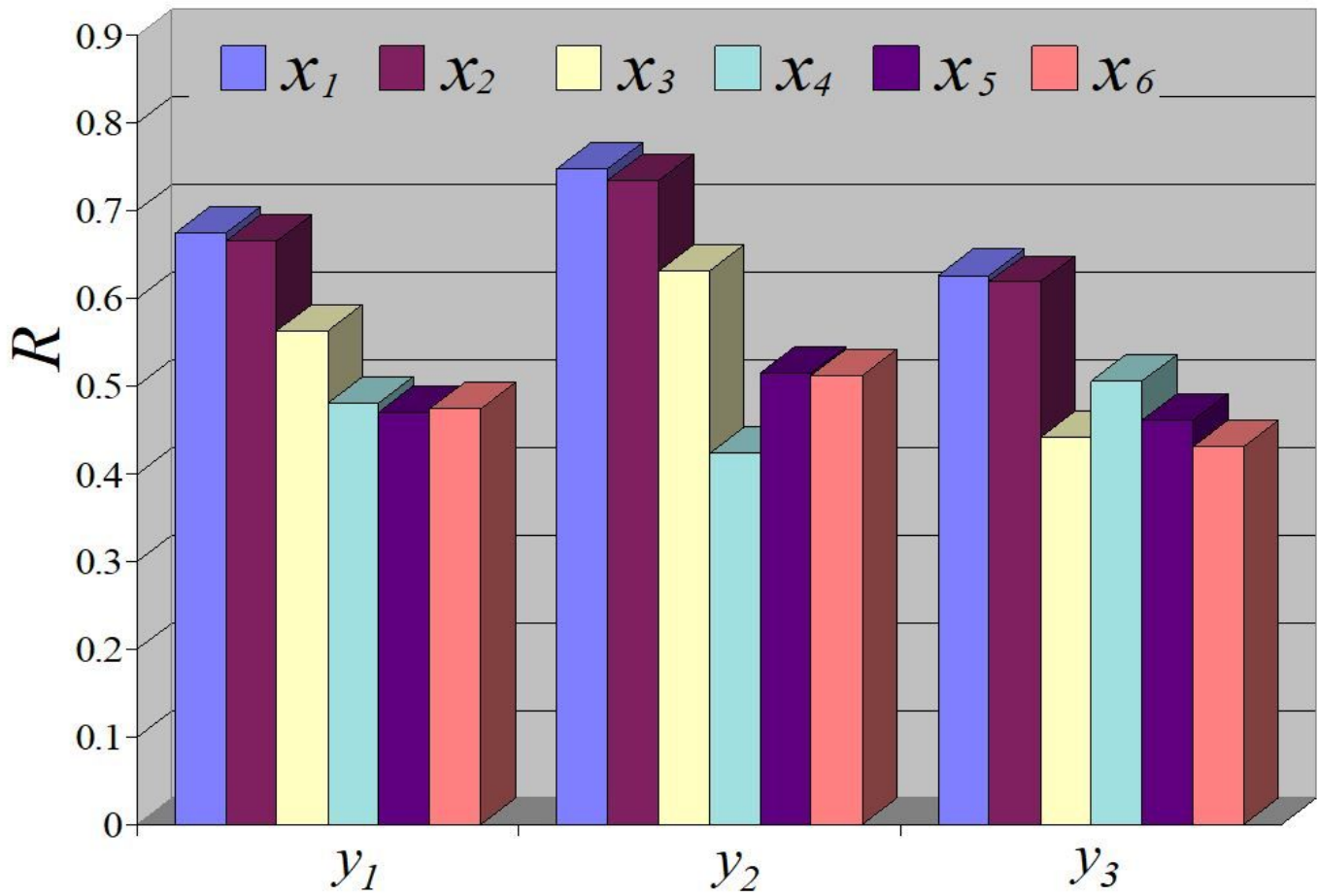


Figure 16

Influence correlation degree